Electron Spin Resonance Spectroscopy

Bert M. Weckhuysen[1] · Ralf Heidler[2] · Robert A. Schoonheydt[2]

[1] Departement Anorganische Chemie en Katalyse, Debye Instituut, Universiteit Utrecht, Sorbonnelaan 16, 3508 TB Utrecht, The Netherlands

[2] Centrum voor Oppervlaktechemie en Katalyse, Departement Interfasechemie, K.U. Leuven, Kasteelpark Arenberg 22, 3001 Heverlee, Belgium

Abstract. The theoretical principles of the ESR technique and its application in the field of molecular sieve science are reviewed. The first part of this chapter focuses on the basic principles and instrumentation of the ESR, ENDOR, ESE and ESEEM techniques. Special attention will be given to spectral simulation and quantitative analysis of ESR spectra. In the second part, the general features of the ESR spectra of transition metal ions and paramagnetic clusters in molecular sieves are presented and discussed. In addition, some remarks will be made about the use of paramagnetic molecules, such as NO.

1
Introduction

Electron spin resonance (ESR) spectroscopy is a very powerful and sensitive method for the characterization of the electronic structures of materials with unpaired electrons. There is a variety of ESR techniques, each with its own advantages. In continuous wave ESR (CW-ESR), the sample is subjected to a continuous beam of microwave irradiation of fixed frequency and the magnetic field is swept. Different microwave frequencies may be used and they are denoted as S-band (3.5 GHz), X-band (9.25 GHz), K-band (20 GHz), Q-band (35 GHz) and W-band (95 GHz). Other techniques, such as electron nuclear double resonance (ENDOR) and electron spin echo envelope modulation (ESEEM) spectroscopies, record in essence the NMR spectra of paramagnetic species.

Electron spin resonance and related techniques have been applied in molecular sieve science for the characterization of transition metal ions that are present in the lattice and on the surface, coordinated to lattice oxygen atoms or to extra-lattice ligands. The technique is also applied to paramagnetic clusters, mainly of silver and alkaline metals and, in rare cases, to adsorbed paramagnetic molecules such as NO to probe defects and Lewis acidity. Because ESR spectra of transition metal ions are often characterized by interactions which are no longer small compared with the electron Zeeman interaction, one cannot use perturbation theory of the first order to evaluate the spectra. Therefore, extensive spectral simulation is required to extract physically meaningful ESR parameters. Such information is a necessity for a detailed description of the coordination geometry of zeolitic transition metal ions. ESR is also a very sensitive technique, but quantitative analysis can only be done with good standards within 10 to 20% accuracy.

This review deals with both the theoretical and practical aspects of the use of ESR spectroscopy in molecular sieve science. No attempt has been made to compile an exhaustive list of references to all the work that has been published so far. Rather, we have selected what, we feel, are the most important developments and also, where possible, we have drawn examples from our own work. In a first part, the ESR technique and its extensions such as ENDOR and ESEEM, will be highlighted with special emphasis on the principles of the techniques and the instrumental requirements. Attention will also be given to spectral simulation and to quantitative analysis. In a second part, the general features of ESR spectra of transition metal ions in molecular sieves are analyzed. In addition, some remarks will be made on paramagnetic metal clusters and on paramagnetic molecules. The chapter closes with general conclusions and an outlook into the future. For detailed explanations and discussions-in-depth, we refer to several excellent text books [1–9] and review papers [10–14].

2
Principles and Practice of ESR

2.1
Basic Principles and Magnetic Interactions

Electron spin resonance is a magnetic resonance technique, based on the interaction of unpaired electron spins with an external magnetic field. The essential aspects of ESR may be illustrated by considering the hypothetical case of a single isolated electron. This electron is characterized by the quantum number $S = {}^1/_2$ and possesses a magnetic moment:

$$\vec{\mu}_e = - g_e \cdot \beta_e \cdot \vec{S} \tag{1}$$

with $g_e = 2.0023$, the electron g-factor or Landé-factor, $\beta_e = 9.42 \cdot 10^{-24}$ J.T^{-1}, the electronic Bohr magneton and $\vec{S}$, the dimensionless electron spin vector. In a magnetic field, B_0, there are two energy states for this electron, as illustrated in Fig. 1. This interaction, known as the Zeeman interaction, is expressed by the following Hamiltonian:

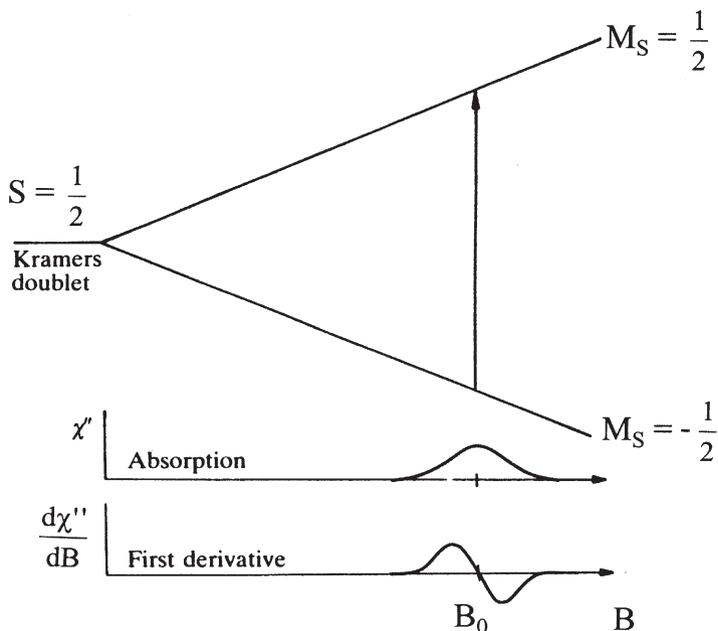$$\bar{H}_{ZI} = - \mu_e \cdot \bar{B} = g_e \cdot \beta_e \cdot B_0 \cdot S_Z \tag{2}$$

Fig. 1. Energy level diagram for an isolated electron in a magnetic field B and the corresponding absorption spectrum and first derivative ESR spectrum (reprinted from reference [2]. Copyright 1990 Oxford University Press)

Two energy levels evolve, viz. $E_\beta = -1/2 g_e \cdot \beta_e \cdot B_0$ and $E_\alpha = +1/2 g_e \cdot \beta_e \cdot B_0$, which are almost equally populated. In ESR spectroscopy, the magnetic component of a microwave energy, which is perpendicular to the magnetic field B_0, induces microwave energy absorption subject to the resonance condition (3) and the selection rule $\Delta M_s = \pm 1$:

$$\Delta E = h \cdot \nu = g_e \cdot \beta_e \cdot B_0 \tag{3}$$

where ν is the microwave frequency.

In real chemical systems, the single unpaired electron is associated with at least one atom and the second contribution to paramagnetism stems from the electron motion in an orbital with orbital angular momentum L. This effect can be described by the following Hamiltonian:

$$\bar{H} = \beta_e \cdot \bar{B} \, (\bar{L} + g_e \cdot \bar{S}) + \lambda \cdot \bar{L} \cdot \bar{S} = \beta_e \cdot \bar{B} \cdot \bar{\bar{g}} \cdot \bar{S} \tag{4}$$

with λ, the spin-orbit coupling constant and g, the effective g-value. The orbitals (atomic or molecular) have two effects: (1) spin-orbit coupling and (2) orbital-magnetic field interaction. These effects explain why g is no longer equal to 2.0023 ($= g_e$) and anisotropic. The anisotropy of the $\bar{\bar{g}}$-tensor leads to orientation-dependent ESR-spectra for single crystals, but for disordered systems as in the case of molecular sieves, one observes the superposition of spectra of all possible orientations of the magnetic field. Idealized ESR patterns, together with their corresponding absorption profile, are given in Fig. 2. The anisotropy in g is classified into isotropic (one g-value), axial (two g-values) and rhombic (three g-values). The deviation of the principal g-values from the free electron value of 2.0023 carries information about the orbital angular momentum of the electron, i.e. information concerning the electronic structure of the atom or molecules.

The magnetic moment of the electron will also undergo additional interactions with local magnetic fields originating from non-zero nuclear spins. This coupling, known as the hyperfine interaction, is given by:

$$\bar{H}_{HF} = \bar{I} \cdot \bar{\bar{A}} \cdot \bar{S} \tag{5}$$

with $\bar{\bar{A}}$ the hyperfine coupling tensor, characterized by three mutually orthogonal principal values A_{xx}, A_{yy} and A_{zz}. The point symmetry of the paramagnetic entity determines whether or not any of the principal axes of g and A are parallel to each other. The different possibilities and the relation with symmetry are summarized in Table 1, together with the generally accepted nomenclature for ESR behavior. The magnetic moment of the electron may also undergo interactions with the local magnetic fields originating from non-zero nuclear spins of atoms in the first coordination sphere around an atom with unpaired electron. This interaction, called superhyperfine splitting, is mostly weak and unresolved.

Some nuclei with nuclear spins $I \geq 1$ possess an electric quadrupole moment eQ because of the non-spherical charge distribution in the nucleus. The interaction with such nuclei may be expressed as:

$$\bar{H}_Q = \bar{I} \cdot \bar{\bar{Q}} \cdot \bar{I} \tag{6}$$

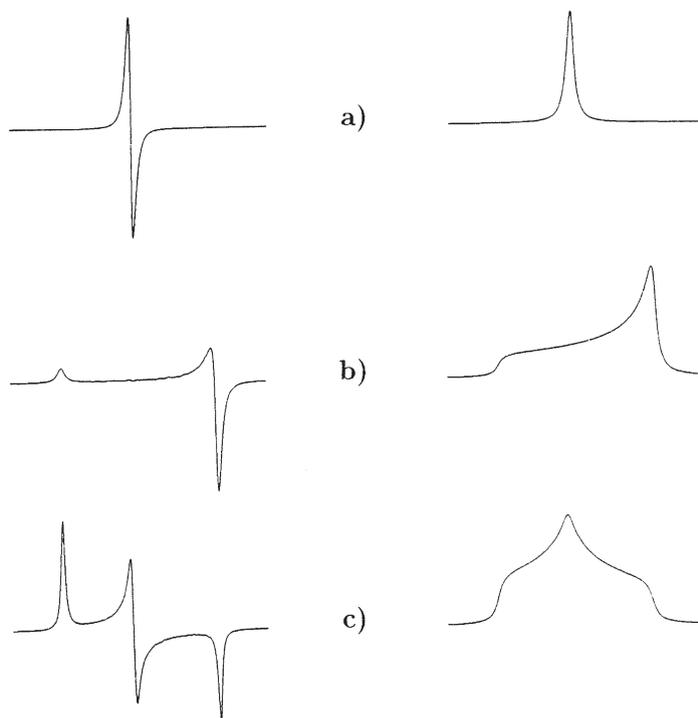with $\bar{\bar{Q}}$ the quadrupole coupling tensor.

Fig. 2a–c. Idealized powder ESR patterns, together with their corresponding absorption profile: **a** isotropic; **b** axial and **c** rhombic

Table 1. Relationships between g and A tensors, ESR symmetry and the point symmetry of paramagnets

ESR symmetry	g and A tensors	Coincidence of tensor axes	Molecular point symmetry
Isotropic	$g_{xx}=g_{yy}=g_{zz}$ $A_{xx}=A_{yy}=A_{zz}$	all coincident	O_h, T_d, O, T_h, T
Axial	$g_{xx}=g_{yy}\neq g_{zz}$ $A_{xx}=A_{yy}\neq A_{zz}$	all coincident	D_{4h}, C_{4v}, D_4, D_{2d}, D_{6h}, C_{6v}, D_6, D_{3h}, D_{3d}, C_{3v}, D_3
Rhombic	$g_{xx}\neq g_{yy}\neq g_{zz}$ $A_{xx}\neq A_{yy}\neq A_{zz}$	all coincident	D_{2h}, C_{2v}, D_2
Monoclinic	$g_{xx}\neq g_{yy}\neq g_{zz}$ $A_{xx}\neq A_{yy}\neq A_{zz}$	one axis of g and A coincident	C_{2h}, C_s, C_2
Triclinic	$g_{xx}\neq g_{yy}\neq g_{zz}$ $A_{xx}\neq A_{yy}\neq A_{zz}$	complete non-coincidence	C_1, C_i
Axial non-collinear	$g_{xx}\neq g_{yy}\neq g_{zz}$ $A_{xx}\neq A_{yy}\neq A_{zz}$	only g_{zz} and A_{zz} coincident	C_3, S_6, C_4, S_4, C_{4h}, C_6, C_{3h}, C_{6h}

As in the case of the magnetic moment of the electron, also the magnetic moment of the nucleus interacts with the magnetic field $\vec{B}$. This causes a further term in the spin Hamiltonian:

$$\bar{H}_{NZ} = -g_N \cdot \beta_N \cdot \vec{B} \cdot \bar{I} \tag{7}$$

with β_N the nuclear magneton and g_N the nuclear g-factor which is characteristic for each isotope. Usually this term is negligible in regular ESR, but important in ENDOR spectroscopy.

If two or more unpaired electrons are present, so that the total spin S of the electron system is greater than $^1/_2$, one has to take into account the interaction of the electrons with the electric field generated by the surrounding atoms (i.e. the crystal field or ligand field). This interaction causes a splitting of the more than twofold (Kramers-) degenerated ground state of the electron system even in the absence of an external magnetic field (i.e. zero field splitting). This interaction results in a line splitting in the ESR spectrum and this interaction can be described by the following Hamiltonian:

$$\bar{H}_{FS} = \bar{S} \cdot \bar{\bar{D}} \cdot \bar{S} \tag{8}$$

with the fine structure tensor $\bar{\bar{D}}$. The Hamiltonian becomes [2–5]:

$$\bar{H}_{FS} = D\left(\bar{S}_z^2 - \frac{S(S+1)}{3}\right) + E\left(\bar{S}_x^2 - \bar{S}_y^2\right) \tag{9}$$

Here D denotes the axial fine structure parameter, whereas E describes the orthorhombic fine structure parameter [5]. The influence of an axial (i.e. $D{\neq}0$ and $E{=}0$) and an orthorhombic fine structure splitting (i.e. $D{\neq}0$ and $E{\neq}0$) on a powder spectrum is shown in Fig. 3 for an isotropic g-tensor and for S equal to $^3/_2$ (e.g. Cr^{3+}).

Summarizing, four different magnetic interactions may occur, which influence the behavior of electrons in a magnetic field: (a) the Zeeman interaction, $\bar{H}_{ZI}$; (b) the nuclear hyperfine interaction, $\bar{H}_{HF}$; (c) the electrostatic quadrupole interaction, $\bar{H}_Q$ and (d) the zero-field splitting if $S > ^1/_2$, $\bar{H}_{FS}$. The sum of these interactions results in the total spin Hamiltonian, $\bar{H}_T$:

$$\bar{H}_T = \beta_e \cdot \vec{B} \cdot \bar{\bar{g}} \cdot \bar{S} + \bar{I} \cdot \bar{\bar{A}} \cdot \bar{S} + \bar{I} \cdot \bar{\bar{Q}} \cdot \bar{I} + \bar{S} \cdot \bar{\bar{D}} \cdot \bar{S} \tag{10}$$

2.2
Instrumentation and Signal Generation

The basic components of an ESR spectrometer are shown in Fig. 4 [15]. The microwave bridge supplies microwaves at a fixed frequency and chosen power, however, the microwave frequency is tuneable over a limited frequency range. The microwave source is a klystron or a gundiode. If one wishes to obtain ESR spectra at different frequencies, then a wide range of microwave sources need to be called in. The most commonly used and commercially available frequency is
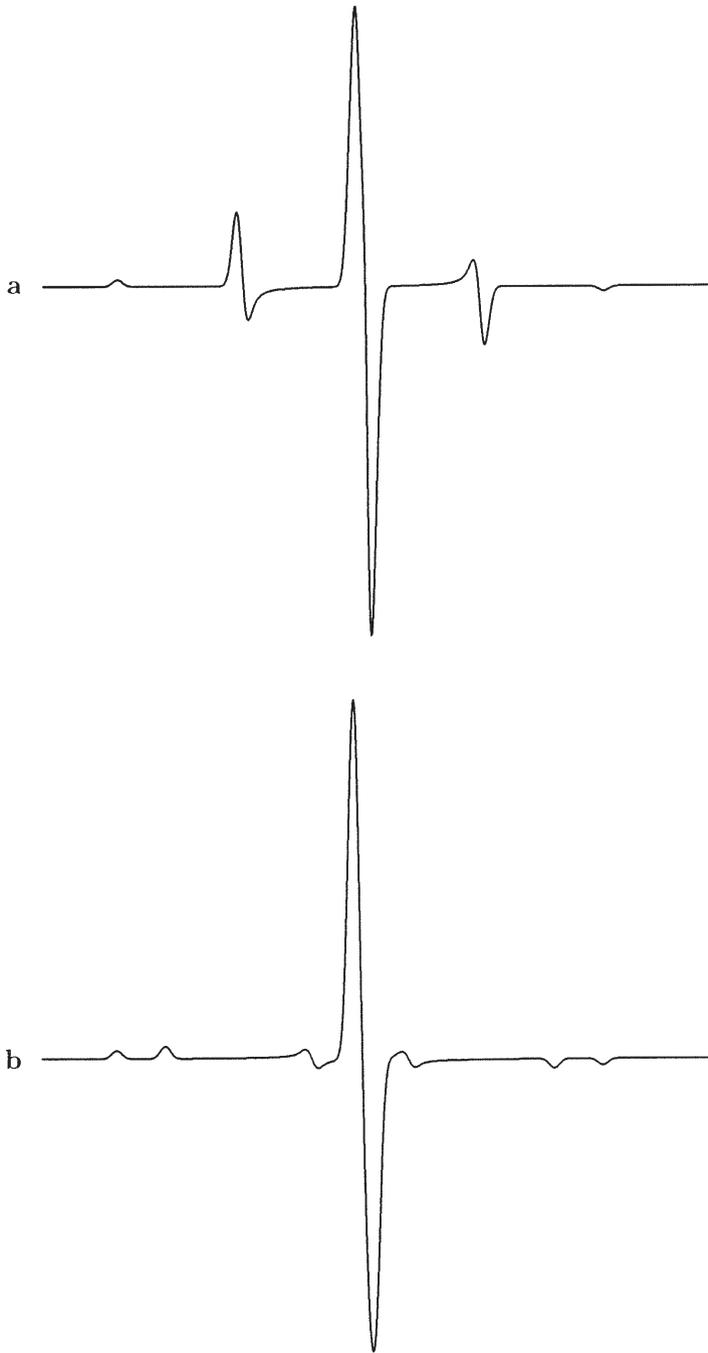
Fig. 3a, b. Influence of the zero field parameters D and E on a powder ESR spectrum with $S = {}^3/_2$: **a** $D \neq 0$; $E = 0$ and **b** $D \neq E \neq 0$

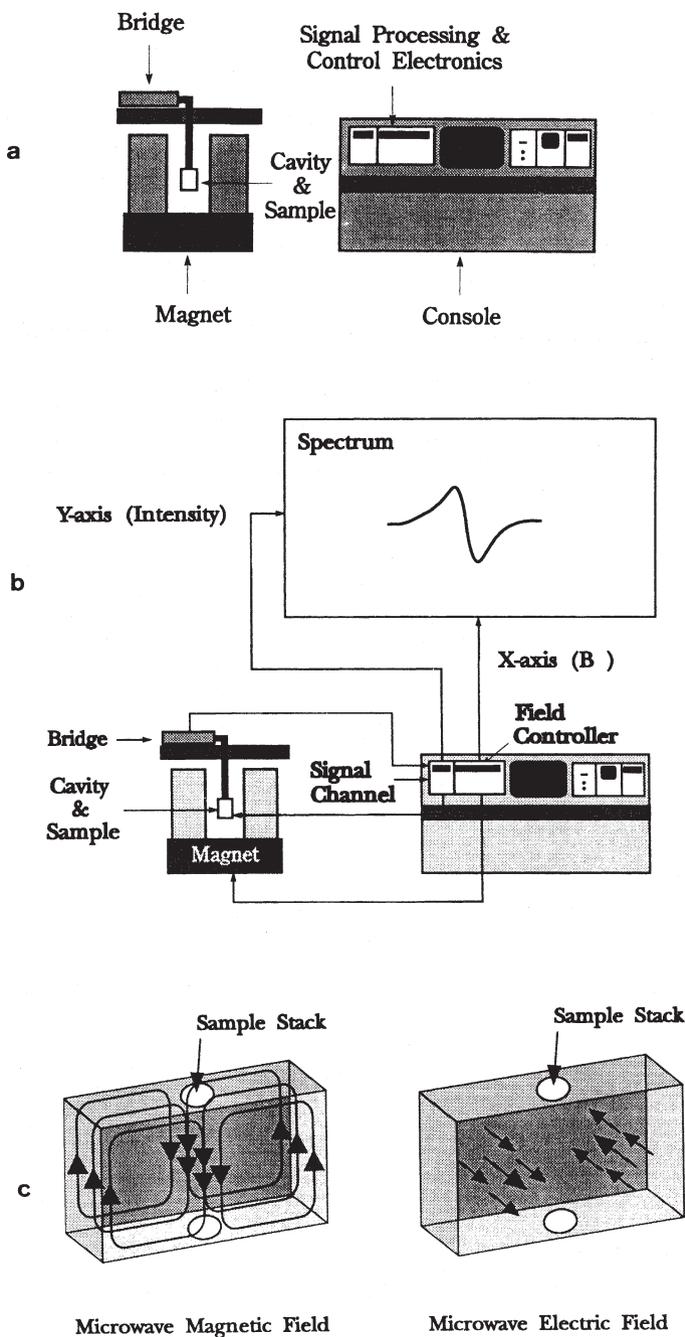**Fig. 4a–c.** **a** General layout of an ESR spectrometer; **b** Block diagram of an ESR spectrometer and **c** Magnetic and electric field patterns in a standard ESR cavity (reprinted from reference [15]. Copyright 1992 Bruker Instruments, Inc.)

ca. 9.25 GHz (X-band) and the corresponding resonance field for $g = 2$ is 0.3300 T. Q-band ESR, at ca. 35 GHz, is the next commonly used frequency, which gives transitions at 1.2500 T for $g = 2.0$. More recently, a commercial W-band ESR spectrometer (ca. 90 GHz) became available and it is expected that it will add significantly to our understanding of zeolite materials. The microwaves are transmitted to a sample cavity via a waveguide. The sample cavity is a device in which the sample can be irradiated with the microwave energy, but which is also capable of being tuned so that microwave energy can be reflected back to a detector in the microwave bridge. The design of the cavity depends mainly on the applied microwave frequency because the dimensions of the cavity (and waveguide) must match the wavelength of the microwaves. The wavelength (and cavity dimensions) for X- and Q-band are 3.24 and 0.86 cm, respectively. It is also clear that these size limitations have a strong influence on the maximum amount of sample that a particular cavity will tolerate. For example, Q-band cavities permit only the use of very small amounts of samples. The sample cavity is then placed perpendicular to the applied magnetic field, B_0, which can be varied in a controlled way. B_0 is generated by an electromagnet and should be as accurate and homogeneous as possible. In addition to the main magnetic field a controlled but smaller oscillating magnetic field is superimposed on the sample cavity via the modulation coils. Thus, the signal response from the cavity is modulated at the modulation frequency, and a first derivative ESR spectrum results. The ideal way to perform an ESR experiment would be to apply a fixed magnetic field and to vary the microwave frequency. However, as discussed above, microwave sources are tunable only over limited ranges. Therefore, the microwave frequency is kept constant and the applied magnetic field is varied over a field range in which microwave absorption is expected. This is called continuous wave electron spin resonance (CW-ESR). At the stage of microwave absorption, a change of the intensity of the reflected microwave energy is detected by a detector and the signal obtained is amplified, recorded and stored for further treatment.

The following parameters must be optimized to obtain a physically meaningful ESR spectrum:

(i)   magnetic field scan range: If you do not know much about your sample, it is advisable to scan the widest magnetic field range available, i.e. from zero up to the maximum. Afterwards, one may pick up the scan range of interest;

(ii) modulation amplitude: An oscillating magnetic field at a fixed and stable frequency (mostly 100 kHz) is applied to the sample cavity via coils. The magnetic field is applied continuously throughout the experiment. The amplitude of this modulation is very important because high modulation amplitudes may distort the individual lines in a spectrum so that valuable information is lost. This is especially important when the lines are sharp and weak.

(iii) sweep time: Short sweep times may significantly distort the ESR spectrum in that (a) the cross-over point of the first derivative spectrum may be shifted in the direction of the scan; (b) the spectrum becomes asymmetric or (c) the signal intensity reduces.

(iv) sample temperature: Low concentrations of paramagnetic entities may become only visible at low measuring temperature. Furthermore, measurements of the signal intensity as a function of the sample temperature allow one to distinguish different types of magnetic behavior (i.e. paramagnetism, anti-ferromagnetism, etc.);

(v) microwave power: At low values of the microwave power, the signal amplitude will increase in direct proportion to the square root of the microwave power received by the sample. This relationship, however, is only obeyed up to a certain power level, beyond which the signal intensity levels off or even decreases. This is known as microwave power saturation and no quantitative information can be extracted from saturated spectra. Saturation effects are also more pronounced at low temperatures.

If one wants to determine g-values from ESR spectra, one has to know both the field B_0 and the microwave frequency (Eq. 3). There are two possible methods: One can use a Gaussmeter and a frequency counter, both of which are relatively expensive instruments; the second method is based on the use of a standard with accurately known g-values. A double rectangular cavity (TE_{104}) is very convenient in that the standard (REF) is placed in one half of the cavity and the (unknown) sample (M) in the other. Only one cavity tuning operation is necessary for both measurements. With DPPH (diphenylpicrylhydrazine) as standard with $g_{REF} = 2.0036$, one has:

$$h \cdot \nu_{REF} = g_{REF} \cdot \beta \cdot B_{0,REF} \tag{11}$$

$$h \cdot \nu_M = g_{eff} \cdot \beta \cdot B_{0,M} \tag{12}$$

with

$$h \cdot \nu_{REF} = h \cdot \nu_M \tag{13}$$

or

$$g_{eff} = g_{REF} \cdot (B_{0,REF}/B_{0,M}) \tag{14}$$

The resonance fields $B_{0,REF}$ and $B_{0,M}$ are read directly from the ESR spectra.

2.3
Quantitative Analysis

The concentration, C, of a paramagnetic entity in a sample, subjected to an ESR experiment, is given by Eq. (15) [5]:

$$C = \frac{K \cdot I}{G \cdot P} \tag{15}$$

with K, a proportionality constant; I, the ESR line intensity; G, the amplifier gain of the spectrometer and P, the ESR transition probability [5]. The proportionality constant K is dependent on (a) the properties of the sample cavity, (b) the applied microwave power and (c) the applied modulation amplitude. The intensity I of the ESR signal must be obtained by working in the linear region of the microwave detectors and in the absence of microwave power saturation (i.e. low

paramagnetic concentrations). It is important to stress that an ESR signal consists of the first derivative of the absorption line and the ESR intensity must be related with the area under the absorption envelope. This is done by double integration of the recorded first derivative spectrum over a well-defined scan range.

If the number of spins in a standard is accurately known, its signal intensity can be used to determine the number of spins in the unknown sample. It is clear that K and P of Eq. (15) must be identical for the standard and the (unknown) sample. The related implications are that the conditions (a) to (c) should be identical for the paramagnetic sample and for the standard. Condition (a) means that the sample container, the volume of sample, the positioning in the sample cavity and the dielectric properties of both samples are identical. In addition, the standard should ideally have ESR properties (electronic structure, g-values, etc.) identical to those of the studied paramagnetic entity. Because this is almost impossible, one should choose a standard which is as close as possible to that of the unknown (e.g. Cu^{2+} (d^9) for Cr^{5+} (d^1) -quantification) [16].

If the ESR spectra of the paramagnetic entity in the unknown sample (M) and of the standard or reference compound (REF) have the same number of features spread over the same magnetic field range and if these spectra are integrated over the same scan range, then ESR allows the quantification of this paramagnetic entity according to Eq. 16:

$$N_M = N_{REF} \cdot \left(\frac{A_M}{A_{REF}} \right) \cdot \left(\frac{g_{REF}}{g_M} \right) \cdot \left(\frac{S_{REF} \cdot (S_{REF} + 1)}{S_M \cdot (S_M + 1)} \right) \tag{16}$$

with: N_M, N_{REF} = amount of spins of M and reference compound, respectively; A_M, A_{REF} = intensity of the ESR signal of M and reference compound obtained after double integration, respectively; g_M, g_{REF} = g-value of M and reference compound, respectively and S_M, S_{REF} = spin quantum number of M and reference compound, respectively. The last term in Eq. (16) corrects for the differences between the spin quantum number of the unknown and that of the reference compound.

Double integration of the ESR signal is not straightforward, especially in the case of transition metal ions with their spectra smeared out over a broad magnetic field range. The following parameters must be known or chosen:

(i)   Lineshape: This can be Gaussian, Lorentzian or a combination of both.
(ii) Baseline: Integration is always very sensitive to baseline effects. A constant offset, for example, which means that the whole spectrum is shifted up or down from zero, results in a quadratic baseline in the doubly integrated spectrum. If integration is carried out over a wide range, such effect becomes large. This can be corrected by choosing a suitable baseline correction (cubic, linear, etc.).
(iii) Integration width: Each spectrum must be integrated over the same scan range so that the same features are taken into account. Furthermore, large integration widths are recommended because tailing effects may cause important contributions to the overall spectrum.

It may be clear that a quantitative determination of paramagnetic species is rather complicated and requires a great deal of experimental care. Therefore, absolute determination of paramagnetic entities, especially transition metal ions, can only be done within 10 to 20% accuracy and explains why the number of quantitative ESR studies in molecular sieve science is rather limited [12,16].

2.4
Spectrum Simulation

For the simulation of ESR spectra one has to solve the spin Hamiltonian of Eq. (10). The easiest way to do this is to regard all the different terms in the spin Hamiltonian as small compared with the electron Zeeman interaction and to use perturbation theory of the first order. The Zeeman term can easily be solved within the eigensystem of the S_Z operator (in the main axis system of the g-tensor or $\vec{S}_Z = \vec{B}$ for isotropic cases), for instance in the isotropic case:

$$E^Z = g \cdot \beta \cdot B \cdot m_S \tag{17}$$

Unfortunately, in most cases this simplification is not applicable. Therefore, the use of perturbation theory of higher order is recommended, or in more complicated situations, the diagonalization of the spin Hamiltonian within the eigensystem of its spin operators.

Because the ESR experiment does not measure the energy spectrum for one fixed magnetic field by scanning the frequency of the microwave, but scans the magnetic field, it is necessary to calculate the energy levels for each magnitude of the magnetic field and to determine the resonance fields by comparing the differences of the energy levels with the applied microwave energy. Therefore, the spin Hamiltonian needs to be diagonalized very often and such calculations are time consuming. For the calculated resonance positions, it is easy to determine the appropriate intensities by evaluating the transition probabilities which can be calculated using the eigenfunctions of the spin Hamiltonian.

For disordered systems (e.g. powders), as usual in molecular sieve science, the contributions of all possible orientations of the magnetic field has to be taken into account. This is illustrated in Fig. 5. Thus, the above described calculations need to be summed up for all orientations (i.e. integration about φ in the axial case and about φ and ϑ in orthorhombic systems). Eventually the line shape has to be taken into account by convolution of the result with the appropriate line shape function (e.g. Gaussian or Lorentzian line with a suitable line width). There are a lot of simulation programs available in literature, either based on perturbation or matrix diagonalization methods: MAGRES (from the Department of Molecular Spectroscopy in Nijmegen, The Netherlands); MSPEN/MSGRA (from the group of Hütterman in Hamburg, Germany); QPOW (from the group of Belford, University of Illinois, USA); EPR.FOR (from the group of Weil, University of Saskatchewan, Canada), Manchester program (from the group of Mabbs and Collison, Manchester University, UK) and Pilbrow program (from the group of Pilbrow, Monash University, Australia). Details about these programs can be found in the text book by Mabbs and Collison [5].
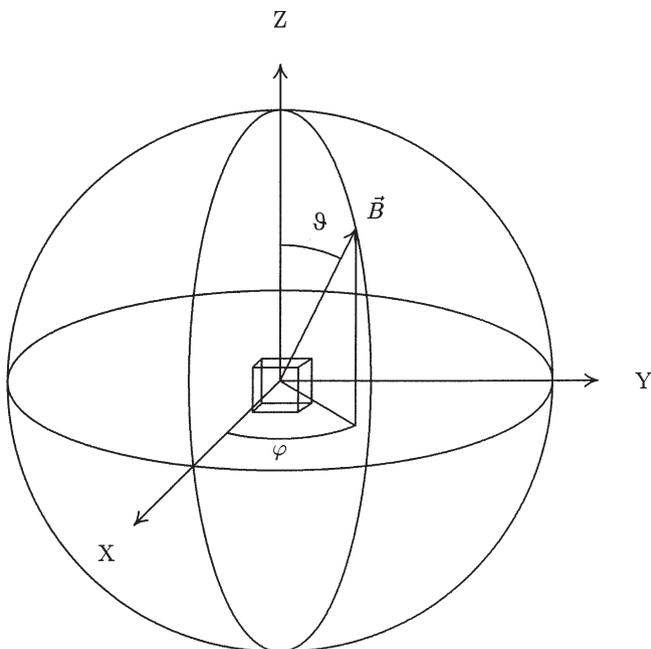
Fig. 5. Definition of the polar angles of the applied magnetic field, B_0, with their respect to the principal axes

In practice one usually wishes to determine accurately the parameters of the spin Hamiltonian out of the measured spectrum. Therefore one has to estimate the parameters (g, D, E, A, Q, the line shape and the line width) to simulate the spectrum and to compare the result with the experimental spectrum, eventually followed by re-estimation of the parameters and simulation.

2.5
Modern ESR-Related Techniques: ENDOR and Pulsed ESR

The classic ESR technique, although very powerful, frequently suffers from inhomogeneous line broadening as a consequence of dipolar interactions and gives rise to poorly resolved ESR spectra. A considerable enhancement in resolution may be obtained by applying modern ESR-related techniques, which are capable of measuring nuclear magnetic transition frequencies in paramagnetic systems. In this paragraph two of these more advanced techniques will be discussed, i.e. electron nuclear double resonance (ENDOR) and a pulse variant of CW-ESR, electron spin echo spectroscopy (ESE). Detailed reviews on these techniques and their applications are available in the literature [17–24].

2.5.1
Electron Nuclear Double Resonance (ENDOR)

In ENDOR spectroscopy, one measures the NMR spectrum of nuclei which interact with a paramagnetic center. The principle of ENDOR spectroscopy is illustrated by Fig. 6 for a system with both S and I equal to $^1/_2$ (consider, e.g., a one electron – one proton two spin system, i.e. with one electron and one nuclear spin). The Hamiltonian operator, which is appropriate for this case ($I=^1/_2$, i.e. $eQ=0$; $S=^1/_2$, i.e. $D=0$; H_{NZ} non-negligible; see Eqs. (1), (2), (5), (7), (10)) is given by

$$\bar{H}_T = \beta_e \cdot \bar{B} \cdot \bar{\bar{g}}_e \cdot \bar{S} + \bar{I} \cdot \bar{\bar{A}} \cdot \bar{S} - g_N \cdot \beta_N \cdot \bar{B} \cdot \bar{I} \qquad (18)$$

This operator has to be applied on the eigenfunctions of the spin system, (one electron-one proton two-spin system), i.e. on $\varphi_4 = |\alpha_e \cdot \alpha_n\rangle$, $\varphi_2 = |\alpha_e \cdot \beta_n\rangle$, $\varphi_2 = |\beta_e \cdot \beta_n\rangle$, $\varphi_1 = |\beta_e \cdot \alpha_n\rangle$; with $\alpha_e, \beta_e, \alpha_n, \beta_n$ indicating the eigenfunctions of the electron (e) spin or nuclear (n) spin with the eigenvalues $m_s = ^1/_2$, $m_s = -^1/_2$, $m_I = +^1/_2$ and $m_I = -^1/_2$, respectively. This application provides the energy of levels 1 to 4 of Fig. 6 as follows (compare, e.g., Ref [23] or Ref. [24]):

$$
\begin{aligned}
E_4 &= \tfrac{1}{2}\, g_e \cdot \beta_e \cdot B + \tfrac{1}{4}\, a - \tfrac{1}{2}\, g_N \cdot \beta_N \cdot B \\
E_3 &= \tfrac{1}{2} \cdot g_e\, \beta_e \cdot B - \tfrac{1}{4}\, a + \tfrac{1}{2}\, g_N \cdot \beta_N \cdot B \\
E_2 &= -\tfrac{1}{2}\, g_e \cdot \beta_e \cdot B + \tfrac{1}{4}\, a + \tfrac{1}{2}\, g_N \cdot \beta_N \cdot B \\
E_1 &= -\tfrac{1}{2}\, g_e \cdot \beta_e \cdot B - \tfrac{1}{4}\, a - \tfrac{1}{2}\, g_N \cdot \beta_N \cdot B
\end{aligned}
\qquad (19)
$$

To detect an ENDOR signal one has to record the ESR spectrum and to choose an appropriate line which has to be (at least partially) saturated (vide infra).
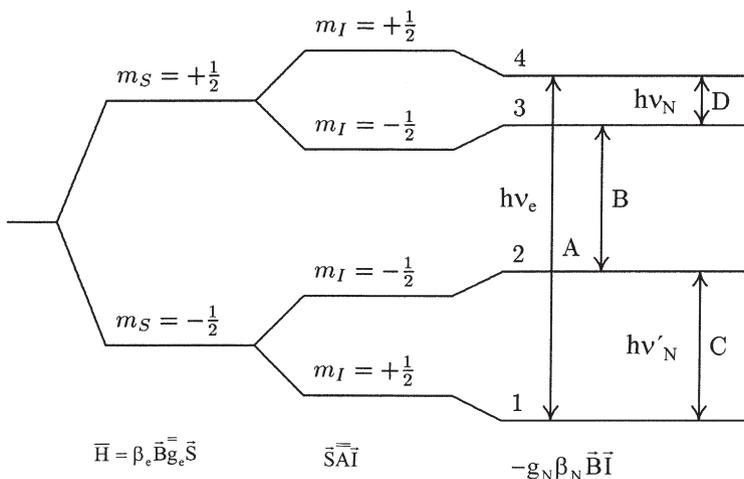

Fig. 6. Energy level scheme for ENDOR

For instance, the allowed ESR transition 1 (1 ↔ 4) can be saturated by application of a sufficiently high microwave power (vide infra) so that the levels 1 and 4 are equally populated and consequently no ESR signal is observed. Now, a strong radiofrequecny field is applied with a frequency, ν_N, given by the energy difference between the levels 3 and 4, i.e.

$$h\nu_N = \tfrac{1}{2}a - g_N \cdot \beta_N \cdot B$$

Thus, NMR transitions D (4 ↔ 3) will be stimulated until the populations of levels 3 and 4 will be equalized. As a consequence, the population of level 4 will slightly decrease. This desaturation enables the ESR signal to re-appear.

Similarly, if a radiofrequency, ν_N, corresponding to the energy difference between levels 1 and 2, i.e.

$$h\nu_N = \tfrac{1}{2}a + g_N \cdot \beta_N \cdot B$$

were employed, NMR transitions C between these levels would be stimulated, again with the result of disturbing the equalized populations of levels 4 and 1, and thus, de-saturating of the electron resonance signal would again occur. In an experiment, where the electron resonance frequency, ν_e, is kept constant and the radiofrequency swept around $\nu_{rf} = {}^1/_{2h}$, the ESR signal will re-appear twice, viz. at

$$\nu_N = \frac{1}{h}\left(\frac{1}{2} - g_N \cdot \beta_N \cdot B\right)$$

$$\nu'_N = \frac{1}{h}\left(\frac{1}{2} + g_N \cdot \beta_N \cdot B\right)$$

From the ENDOR spectrum with these two lines, one can derive both the hyperfine splitting constant, A, and the nuclear factor, g_N (characteristic of given nucleus) with high accuracy.

Though the ENDOR method is a very powerful tool, there are several drawbacks to this method, which sometimes prohibits a successful application. For ENDOR spectroscopy in general an advanced equipment is necessary. Especially the generation of a sufficiently high radiofrequency power and the coils to generate the appropriate magnetic field on the sample are often problematic. Furthermore, the ENDOR effect is usually smaller than the ESR effect (mostly less than one tenth of the ESR intensity) and a sensitive ESR spectrometer is required. In addition, an ENDOR signal can only be detected if one is able to saturate the ESR line at least partially. This means that a low measurement temperature is recommended, usually using liquid helium (4.2 K). Furthermore, the nuclear relaxation time must not be too long to avoid saturation of the NMR transition. The last restrictions can sometimes be circumvented by using pulsed ESR techniques.

2.5.2
Electron Spin Echo Spectroscopy (ESE and ESEEM)

Electron spin echo spectroscopy (ESE) monitors the spontaneous generation of microwave energy as a function of the timing of a specific excitation scheme, i.e. two or more short resonant microwave pulses. This is illustrated in Fig. 7. In a typical two-pulse excitation, the initial π/2 pulse places the spin system in a coherent state. Subsequently, the spin packets, each characterized by their own Larmor precession frequency ω_i, start to dephase. A second π-pulse at time τ effectively reverses the time evolution of the spin packet magnetizations, i.e. the spin packets start to rephase, and an emission of microwave energy (the primary echo) occurs at time 2τ. The echo amplitude, as a function of τ, constitutes the ESE spectrum and relaxation processes lead to an irreversible loss of phase correlation. The characteristic time for the amplitude decay is called the phase memory time T_2^M. This decay is often accompanied by a modulation of the echo amplitude, which is due to weak electron-nuclear hyperfine interactions. The analysis of the modulation frequencies and amplitudes forms the basis of the electron spin echo envelope modulation spectroscopy (ESEEM).

   The main limitation of the above described two-pulse experiment originates from phase relaxation processes. T_2^M may become too short with respect to the instrumental dead time (about 150 ns), resulting in an overlap with the ESE spectrum. This may be overcome by applying a three-pulse excitation scheme (Fig. 7), in which the second pulse of the two-pulse experiment is divided into two π/2
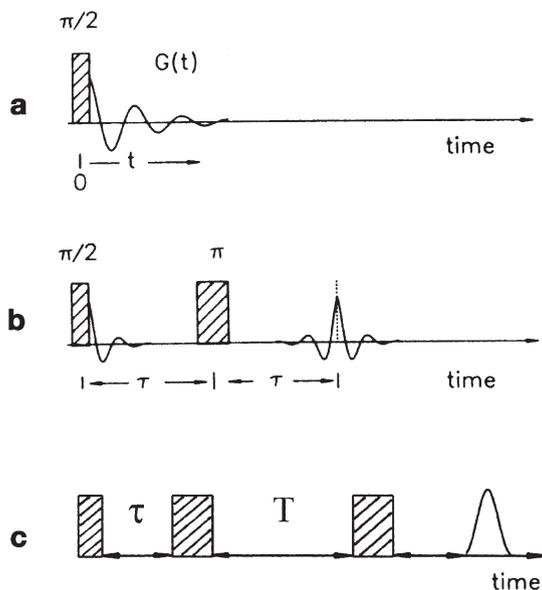

Fig. 7a–c. Pulse sequences for the pulsed ESR technique: **a** single pulse followed by a free induction decay; **b** two pulse sequence; **c** three pulse sequence (reprinted from reference [20]. Copyright 1987 R. Oldenbourg Verlag)

pulses. The echo can now be followed over a time of the order of magnitude $T_1 \gg T_2^M$. With the separation between the first and the second pulse denoted as τ and the one between the second and the third as T, the stimulated echo, occurring at $2\tau+T$, is monitored in the T-space. Thus, there are two experimentally controllable times τ and T. It is therefore possible to suppress one nuclear modulation frequency by appropriate selection of one of these times. The analysis of this modulation provides a way to measure the weak electron-nuclear hyperfine interactions. In addition, it is possible to determine both the number and the distance of magnetic nuclei, surrounding a paramagnetic center.

Three-pulse experiments are well suited for studying the interaction of adsorbed molecules with paramagnetic centers. For example, by selecting the appropriate pulse amplitude, it is possible to observe deuterium modulation, while suppressing proton modulation for adsorbed methanol. This is possible because of the difference in the nuclear frequencies of protons and deuterons. This allows the determination of the orientation of this adsorbed molecule with respect to a paramagnetic center by selective deuteration.

To extract detailed hyperfine information from an ESE spectrum, however, it is necessary to calculate the expected modulation pattern for a certain assumed nuclear geometry. By varying the assumed hyperfine interaction for a simulated modulation pattern until it fits the observed modulation pattern, the weak hyperfine parameters may be determined. The general analysis procedure is to analyze the ESE spectrum in terms of a number of equivalent nuclei located at an average distance from the paramagnetic center. The assumption is then that there is a small overlap of the unpaired electron wave function on the closest nuclei to give an isotropic hyperfine coupling constant A_{iso}.

3
Applications of ESR in Molecular Sieve Science

3.1
Transition Metal Ions

Transition metal ions (TMIs) coordinate to lattice oxygen atoms, form complexes inside the cages and/or channels or occupy framework sites. Classical ESR techniques as well as pulsed ESR, and in particular the analysis of the modulation of the echo envelope signal (ESEEM) has been used extensively to gather detailed information about the coordination environment of TMIs.

3.1.1
Cu^{2+}

In Fig. 8 typical high resolution spectra of Cu^{2+} in dehydrated zeolites are shown. The corresponding ESR parameters (Table 2) are obtained by simulation with an axial spin Hamiltonian, including the Zeeman, the hyperfine and quadrupole interactions, applying second order perturbation. The spectra of Cu-ZSM-5 were obtained from the literature [25–29] and the parameters obtained by visual
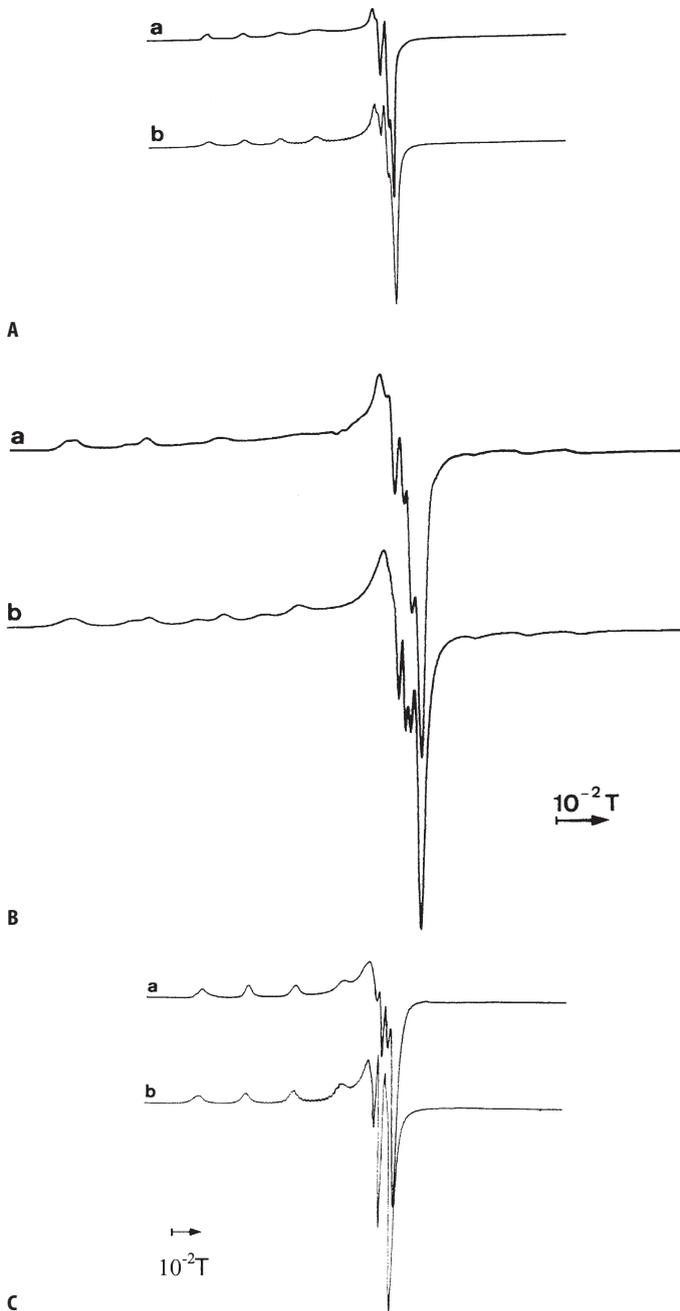
Fig. 8A–D. High resolution ESR spectra of Cu^{2+} in dehydrated zeolites : **A** zeolite A; **B** zeolite X; **C** Mordenite and **D** ZSM-5 (reprinted from reference [26]. Copyright 1993 Marcel Dekker, Inc and from reference [22]. Copyright 1995 American Chemical Society): *a* experimental and *b* theoretical
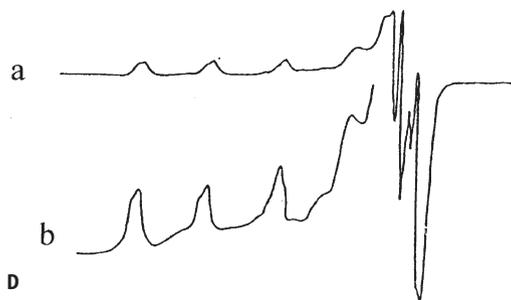
Fig. 8 (continued)

Table 2. ESR parameters of Cu^{2+} in dehydrated zeolites

Zeolite		$g_{||}$	$A_{||}$ (mT)	$g_\perp$	$A_\perp$ (mT)	Q (mT)	Assignment/Location
A		2.386	12.6	2.064	0.25	0.50	A
		2.386	12.6	2.063	1.57	0	re-simulated
X	(1)	2.384	12.7	2.074	1.20	0.33	II
		2.386	12.5	2.069	1.33	0.14	re-simulated
	(2)	2.354	14.3	2.068	1.50	0.35	III'
		2.353	14.4	2.064	1.64	0.00	re-simulated
Y	(1)	2.397	11.9	2.070	1.50	0.30	II
	(2)	2.328	15.5	2.065	1.90	0.32	I'
Mordenite	(1)	2.327	15.4	2.062	1.49	0.26	A
	(2)	2.277	16.8	2.057	1.19	0.28	E
ZSM-5	(1)	2.310	15.0–16.0	–	–	–	square pyramidal
	(2)	2.330	15.0–16.0	–	–	–	square pyramidal
	(3)	2.280	18.0	–	–	–	square planar

inspection. Similar spectra are obtained on Cu^{2+}-loaded SAPO's [30-35]. There are several remarks to be made about the spectra and their simulation:

(1) While a very good guess of the parameters of the parallel region can be obtained from the spectra by visual inspection, this is certainly not the case for the perpendicular region. The reason is that in the parallel region forbidden transitions ($\Delta m_I = \pm 1, \pm 2$) do not contribute to the spectrum, while in the perpendicular region they come into play. They are negligibly small as long as the quadrupole coupling constant Q is small, but become important, as the ratio $|Q|/|A|$ increases. This is illustrated in Fig. 9, showing the perpendicular region of the Cu^{2+}-mordenite spectrum with $g_{||}$=2.327, $A_{||}$=15.5 mT, $g_\perp$= 2.068 and $A_\perp$=1.5 mT. In the first case Q=0.2 mT, in the second case Q=0.5 mT. In the latter case, one notices the increased contribution of the $\Delta m_I = \pm 1$ and $\Delta m_I = \pm 2$ contributions between 0.32 and 0.33 T.
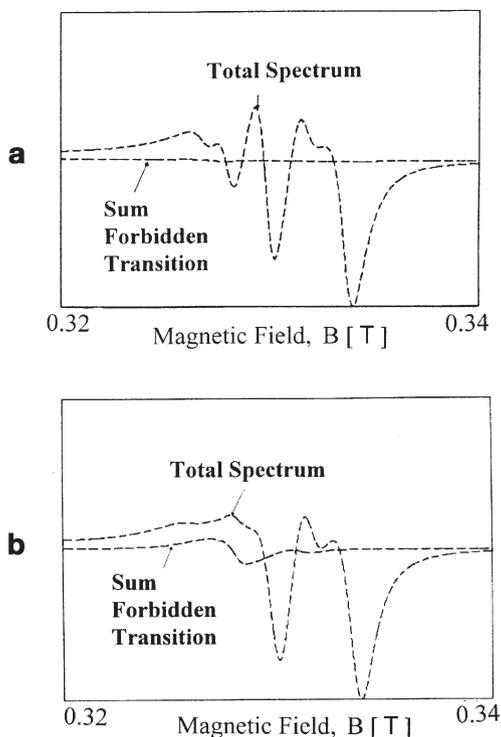
Fig. 9a, b. Effect of the quadrupole coupling constant Q on the ESR spectra of dehydrated Cu mordenite : **a** $|Q|$=0.2 mT and **b** $|Q|$=0.5 mT (reprinted from reference [36])

(2) In powder spectra extra absorptions occur in the perpendicular regions due to significant contributions of paramagnetic centers resonating below 90°. This is illustrated with the absorption spectrum of Cu^{2+}-mordenite in Fig. 10.

The ESR parameters of Cu^{2+} in CuNaA and CuNaX, obtained by simulation with proper account of the forbidden transitions are given in Table 2 [36,37]. The differences are – as expected – more pronounced in the perpendicular region with smaller Q-values and somewhat larger A values. The new parameters are more in line with accepted Cu^{2+} ESR data [26].

We close this discussion by observing that ^{63}Cu and ^{65}Cu nuclei are usually not resolved in the ESR spectra of calcined Cu^{2+}-zeolites. Both nuclei have spin $I=^3/_2$, have relative abundancies of respectively 69.2% and 30.8% and differ slightly in their nuclear Bohr magneton values and quadrupolar moment values. These values are respectively for ^{63}Cu and ^{65}Cu: $\beta_N(^{63}Cu)$=3.743×10^{-27} J · T^{-1}; $\beta_N(^{65}Cu)$=4.005×10^{-27} J · T^{-1}; $Q(^{63}Cu)$=−0.222 e×10^{-24} cm^2 and Q (^{65}Cu)=−0.195 · e×10^{-24} cm^2. Such small differences are often not resolved in the broad powder spectra.

The assignment of the Cu^{2+} spectra to specific sites in dehydrated zeolites is a challenging subject [26]. It has been done with the aid of O_2 line broadening
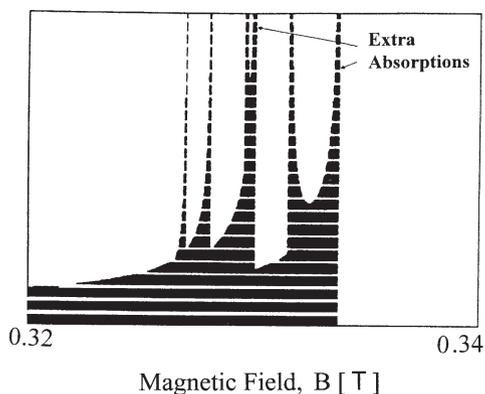
Fig. 10. Effect of the quadrupole coupling constant Q on the ESR spectra of dehydrated Cu mordenite: The perpendicular region in absorption mode shows four hyperfine lines and two extra-absorption lines (reprinted from reference [36])

experiments, with a study of the effect of co-cations on the relative signal intensities, by combination with a study of the d-d transitions and by model calculations in the frame of ligand field and angular model theories. The assignment is given in Table 2. Two remarks can be made here:

(1) The distribution of Cu^{2+} over the sites in faujasite-type zeolites at the typical small loadings of the ESR investigations is not a simple straight line extrapolation from X-ray data (obtained at high loadings only). Common knowledge of zeolite chemistry should have led to the conclusion that at the small loadings of the ESR experiments all Cu^{2+} ions occupy site I. Instead, six-ring sites (I', II) are the preferred ones. There is a strong and short Cu^{2+}-O s-bond in six-ring sites, which cannot be realized in the hexagonal prisms and explains this site preference. An alternative explanation is that Cu^{2+} is asymmetrically located in the hexagonal prisms, i.e. coordinated to three oxygen atoms of one six-ring only, as suggested recently from theoretical calculations on Na^+ [38].

(2) One might also wonder whether at the small loading of 0.25 Cu^{2+}/UC site assignment is possible after all. Do some or all the Cu^{2+} coordinate to the surface at some defect site such as silanol group (>Si-OH+Cu^{2+} $\rightarrow$ >Si-O$^-$-Cu^{2+}+H^+) or others? This cannot be fully ruled out, but the consistency of the data point to real crystallographic Cu^{2+}-siting. Weak background signals, which are always present, might be due to traces of Cu^{2+} at such defects.

A more recent approach on the interpretations of Cu^{2+} spectra to specific cation sites in zeolites is based on the use of *ab initio* calculations [39–41]. The structure of appropriate model clusters of cation sites (e.g. six-ring and five-ring sites) are calculated and optimized with density functional theory. In a next step, the electronic spectra and g-values of the models are calculated. The first results of this approach look very promising and its rigorous application will certainly lead to a better insight into the coordination of transition metal ions in zeolites. An

important conclusions from these studies is that transition metal ions, in particularly Cu^{2+} and Co^{2+}, are able to distort the local environment of a cation site in order to increase their coordination number.

In some cases, especially that of zeolites with high Al content, superhyperfine interaction of Cu^{2+} with the ^{27}Al nucleus ($I=^5/_2$) has been observed. Here, ESEEM is particularly useful [42–44]. When Cu^{2+} is complexed with extra-lattice ligands such as H_2O, methanol, NH_3, ethylenediamine or pyridine, its magnetic moment is effectively screened from the environment. Well resolved spectra can be obtained at much higher Cu^{2+} loadings than for dehydrated zeolites. The ESEEM technique has been pioneered by Kevan and co-workers to detect the weak magnetic interactions between transition metal ions and surrounding nuclei such as H, D and Al. For example, deuterated and ^{13}C-labelled adsorbates have been studied in H-, Na-, K- and Ca-ZSM-5 zeolites by ESR and ESEEM [42]. Simulation of the obtained signals show a fourfold methanol and ethanol coordination of Cu^{2+} in H-ZSM-5, whereas only a threefold coordination is observed in Cu^{2+} exchanged Na-, K- and Ca-ZSM-5. The use of deuterated molecules, such as D_2O and CD_3OH, was also useful in determining the location and structure of Cu^{2+} in zeolites as a function of the co-cation [43–44]. Recently, the technique has been extended to characterize Cu^{2+} complexes in mesoporous MCM-41 [45–46]. Surprisingly, Cu^{2+} was found to bind strongly with surface oxygen atoms and only 2 H_2O, 2 MeOH or 2 NH_3 could enter the coordination sphere, the larger molecules pyridine and benzene being excluded.

In specific cases, the exact composition of the first coordination sphere around Cu^{2+} can be derived from the superhyperfine splitting pattern in ESR. This is illustrated in Fig. 11 for a faujasite-type encaged bisCu(histidine)$_2^+$ complex [47]. The axially symmetric ESR spectrum has a hyperfine splitting with values for $g_\parallel$, $g_\perp$ and $a_\parallel$ of around 2.27, 2.06 and 17 mT, respectively and a seven-line superhyperfine structure with an $A_{N\perp}$ value of 1.23 mT. The additional splitting is due to the presence of three nitrogen atoms ($2 \cdot I_N \cdot n_N+1=7$ with I_N and n_N equal to 1 and 3, respectively) in the first coordination sphere of the Cu^{2+}-ion. This planar NNNO coordination environment was later on confirmed by detailed W-band pulsed ESR techniques [48]. It was also shown that the coordination geometry of
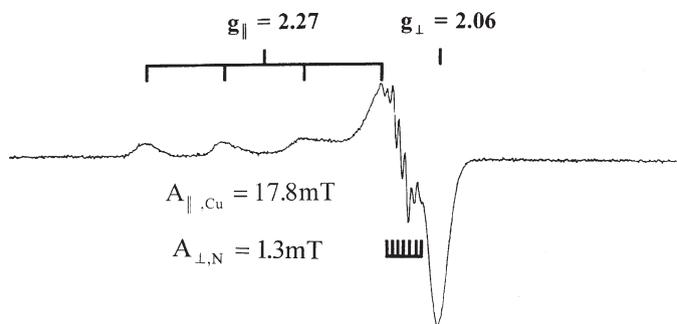

Fig. 11. ESR spectrum of zeolite encaged Cu(histidine)$^{2+}$ (reprinted from reference [47]. Copyright 1995 VCH Verlagsgesellschaft)

these zeolite-encapsulated copper-histidine complexes depend on the Cu^{2+}-loading and, at low Cu^{2+}-loading, a mono $Cu(his)^+$ complex could be formed inside the cages of zeolite Y. ESEEM indicates that this mono-complex is in close contact with the zeolite framework since strong ^{27}Al modulations were observed.

3.1.2
Fe^{3+}

The detection and characterization of Fe^{3+} in molecular sieves by ESR and Mössbauer spectroscopies is almost as old as spectroscopy of molecular sieves itself. Three signals are invariably reported [49–57]:

- a sharp line around $g=4.3$, interpreted as Fe^{3+} in a tetrahedral environment with strong rhombic distortion;
– a broad line around $g=2.3$ due to oxidic Fe species;
– a line around $g=2$, interpreted as Fe^{3+} in (distorted) octahedral environment.

The chemical interpretation of these signals is Fe^{3+} in the lattice, extra-framework Fe_2O_3, Fe^{3+} at exchange sites, respectively. There are many reports in the literature that these interpretations, especially that of the $g=4.3$ signal and that of the $g=2.0$ signal, are not the only possible ones. An alternative interpretation was put forward by Lin et al. in that the three signals were assigned to three different types of framework sites in FAPO-5 [52]. This interpretation has become unlikely in the light of the results of Goldfarb et al. [53–54]. Their interpretation is that the signal at $g=4.3$ is due to Fe^{3+} at defect sites, e.g. silanol groups and that at $g=2.0$ to framework Fe^{3+} and/or Fe^{3+} in exchange sites. The latter signal is ascribed to the $|-^1/_2\rangle \leftrightarrow |^1/_2\rangle$ transition of tetrahedral Fe^{3+}. At the lowest substitution levels (Fe/(Fe+Al)=0.001) the $g=2$ line is sharp and has a weak, broad side-band at low and high fields due to singularities of the other transitions $|-^5/_2\rangle \leftrightarrow |-^3/_2\rangle$, $|-^3/_2\rangle \leftrightarrow |-^1/_2\rangle$, $|^1/_2\rangle \leftrightarrow |^3/_2\rangle$, $|^3/_2\rangle \leftrightarrow |^5/_2\rangle$. If there is more than one crystallographical T site or if the Fe^{3+} content is slightly increased, the $g=2$ line broadens and the weak side bands are not observed anymore. When Fe-sodalite was synthesized with an Fe source enriched in ^{57}Fe, the ^{57}Fe hyperfine splitting constant of 28.7 MHz (10^{-3} T or 9.6×10^{-4} cm^{-1}) was determined by ENDOR.

Several other lines were also reported in the Fe^{3+} ESR spectra of molecular sieves. After solid-state ion exchange of $FeCl_3$-HZSM-5 Kucherov and Slinkin observed up to 7 different signals in the low field region with g-values in the range 9.1–3.4 [55]. In a ferrisilicate three signals with $g=4.25$, 5.2 and 7.9 were observed. When FAPO-5 and ferrisilicalite are hydrothermally synthesized with very low Fe contents (Fe/(Al+P)=$^1/_{1000}$–$^1/_{2000}$; Fe/Si=$^1/_{200}$–$^1/_{100}$) in order to avoid Fe^{3+}-Fe^{3+} interactions, the uptake of Fe in the solid, as measured by ESR matches the development of the crystallinity measured by XRD. Under these conditions at least 5 different signals were observed in X-band ESR and only the relative intensities of the signals vary upon reductive or oxidative treatments [56].

It is impossible to advance an interpretation for all these signals. Computer programs are now available which allow full matrix analysis of the ESR problem of Fe^{3+} instead of the usual perturbative approach. A set of theoretical spectra could be generated for comparison with experimental data [57]. On the other

hand, it is clear that the chemistry of Fe^{3+} in molecular sieves is extremely complicated, both in the synthesis mixtures and on ion exchange sites. We must strive towards very simple chemistry so as to obtain relatively simple spectra which are amenable to theoretical analysis or detailed spectroscopic analysis. Goldfarb et al. [53, 54] have shown the way.

3.1.3
Cr^{5+} and Cr^{3+}

Cr^{5+} (d^1) ESR signals have always axial or rhombic symmetry and typical g-values of zeolitic Cr^{5+} are given in Table 3. On this basis, the signals are assigned to square pyramidal and pseudo-tetrahedral chromyl cations on well-defined ion exchange sites [58–62]. Cr^{5+} in mordenite-type molecular sieves is an interesting example since it is characterized by a complex ESR spectrum (Fig. 12) possessing two rhombic signals with one exhibiting Al superhyperfine splitting (species B). The simulated spectrum, together with the individual components A and B, is also shown in Fig. 12, and is very close to the experimental one [63]. Species A is assigned to Cr^{5+}-ions present at the junction of the main channel and the side pocket, while species B is located near framework aluminum in the main channel of mordenite molecular sieves [64]. Such detailed level of understanding can only be obtained by using specific probe molecules, such as ammonia and pyridine, and also underlines the important role of spectrum simulations.

Three distinguished Cr^{3+} (d^3) ESR signals are observed in molecular sieves, independently of their type and composition [63–66]:

– a broad signal around g_{eff}=2.0, which follows the Curie-Weiss law, assigned to hexaquo Cr^{3+} complexes;

Table 3. ESR parameters of Cr^{5+} in chromium containing molecular sieve and their assignments

| Zeolite	ESR signal	Assignment	Reference
Y	$g_{||}$=1.987; $g_\perp$=1.940 $g_{||}$= 1.980; $g_\perp$=1.915	Y_1-signal : $[Cr=O]^{3+}$-ion at site II (supercage) Y_2-signal : $[Cr=O]^{3+}$-ion at site I' or II' (small cages)	58–60
Mordenite	g_{xx} = 1.9867; g_{yy} = 1.9720; g_{zz} = 1.9110 $g_{||}$=1.9947; $g_\perp$=1.9070	A-signal : square pyramidal $[Cr=O]^{3+}$-ion in the main channel B-signal : distorted tetrahedral $[Cr=O]^{3+}$-ion at junction between main channel and the sidepocket	64
X	$g_{||}$= 1.99; $g_\perp$= 1.93	$[Cr=O]^{3+}$-ion	16
Silicalite	g_{xx} = 4.49; g_{yy}=2.71; g_{zz} = 1.66 g_{xx} = 2.00; g_{yy} 1.67; g_{zz} = 1.66	signal A (substitutional site) signal B (substitutional site)	66
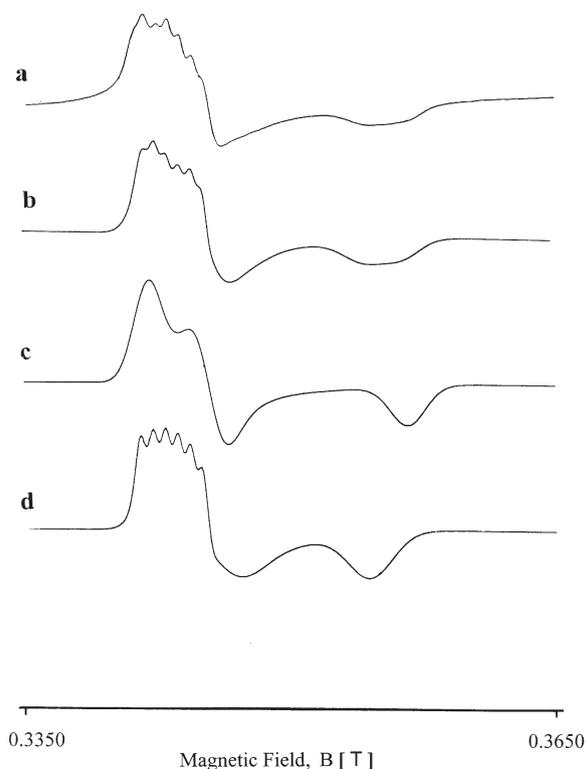
Fig. 12 a–d. ESR spectrum of Cr^{5+} in mordenite: **a** experimental; **b** simulated spectrum obtained by an appropriate summation of the theoretical spectra of species A and B; **c** theoretical spectrum of species A and **d** theoretical spectrum of species B (reprinted from reference [63]. Copyright 1996 The Royal Society of Chemistry)

– a signal around g_{eff}=2.0, which broadens upon cooling, assigned to oxidic Cr^{3+}-clusters;

– a special signal with a broad and positive lobe in the region g_{eff}=4.0–5.5. The origin of this signal has only recently received attention. Detailed spectrum simulations of the Cr^{3+}-system have shown that zero-field parameters D and E need to be introduced into the simulation procedure to obtain spectra with positive lobes in the region g_{eff}=4–5.5. The effect of D and E on the ESR spectra of Cr^{3+} is illustrated in Fig. 13. For D and E equal to zero, only one transition is seen at g_{eff}=2.0. The introduction of small D values gives rise to several transitions at lower and higher g_{eff}-values, while with D equal to 0.5 cm^{-1} effective g-values in the x/y and z direction are obtained around 4.0 and 2.0, respectively. Only by introducing a zero field parameter E of 0.165 cm^{-1}, a clear positive lobe with g_{eff}=4.0–5.5 can be generated. The third signal must therefore be assigned to a strongly distorted Cr^{3+}-species [63]. Similar signals have been observed for Cr supported on amorphous supports and, consequently, they are not unique for zeolitic environments [67].
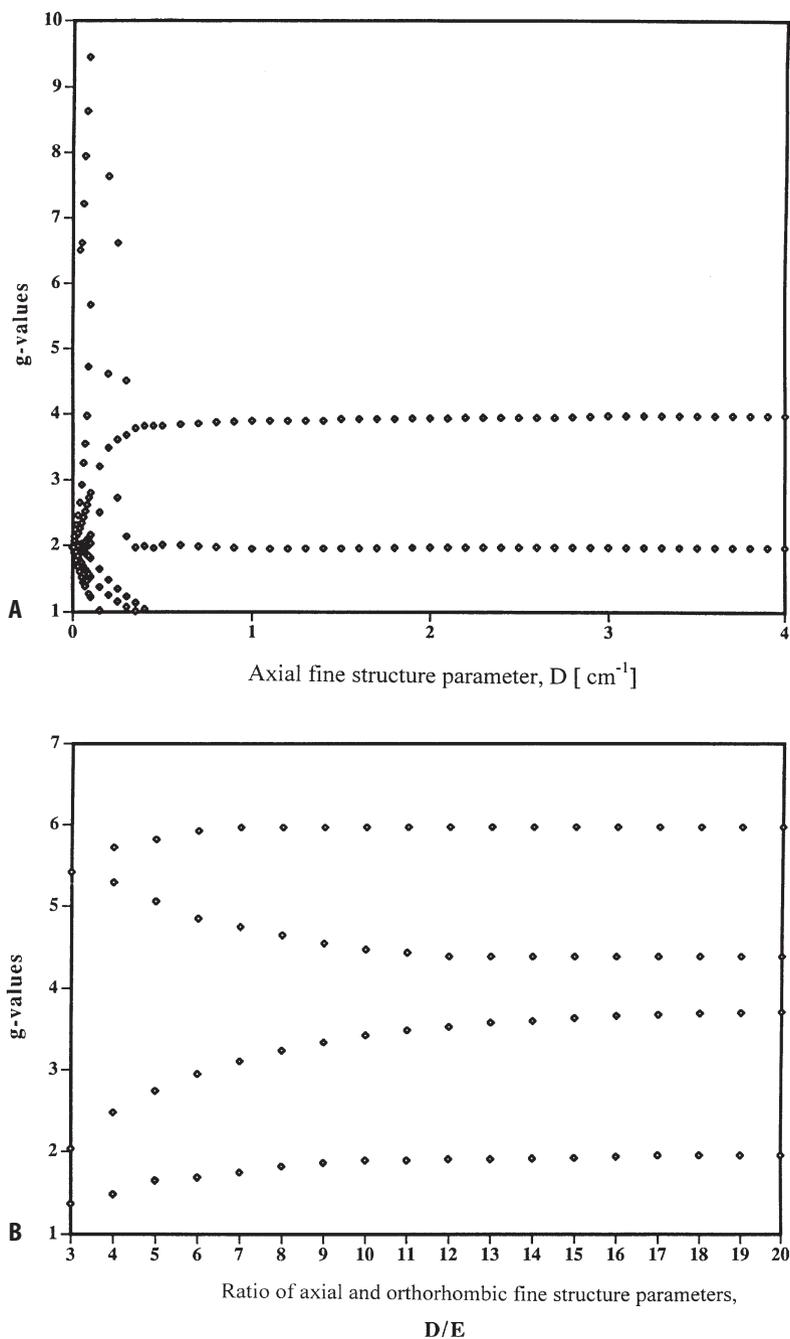
Fig. 13A–D. Influence of zero field parameters D and E on the effective g values of a Cr^{3+}-ion (reprinted from reference [63]. Copyright 1996 The Royal Society of Chemistry: **A** effective g-values as a function of D; **B** effective g-values as a function of D and E

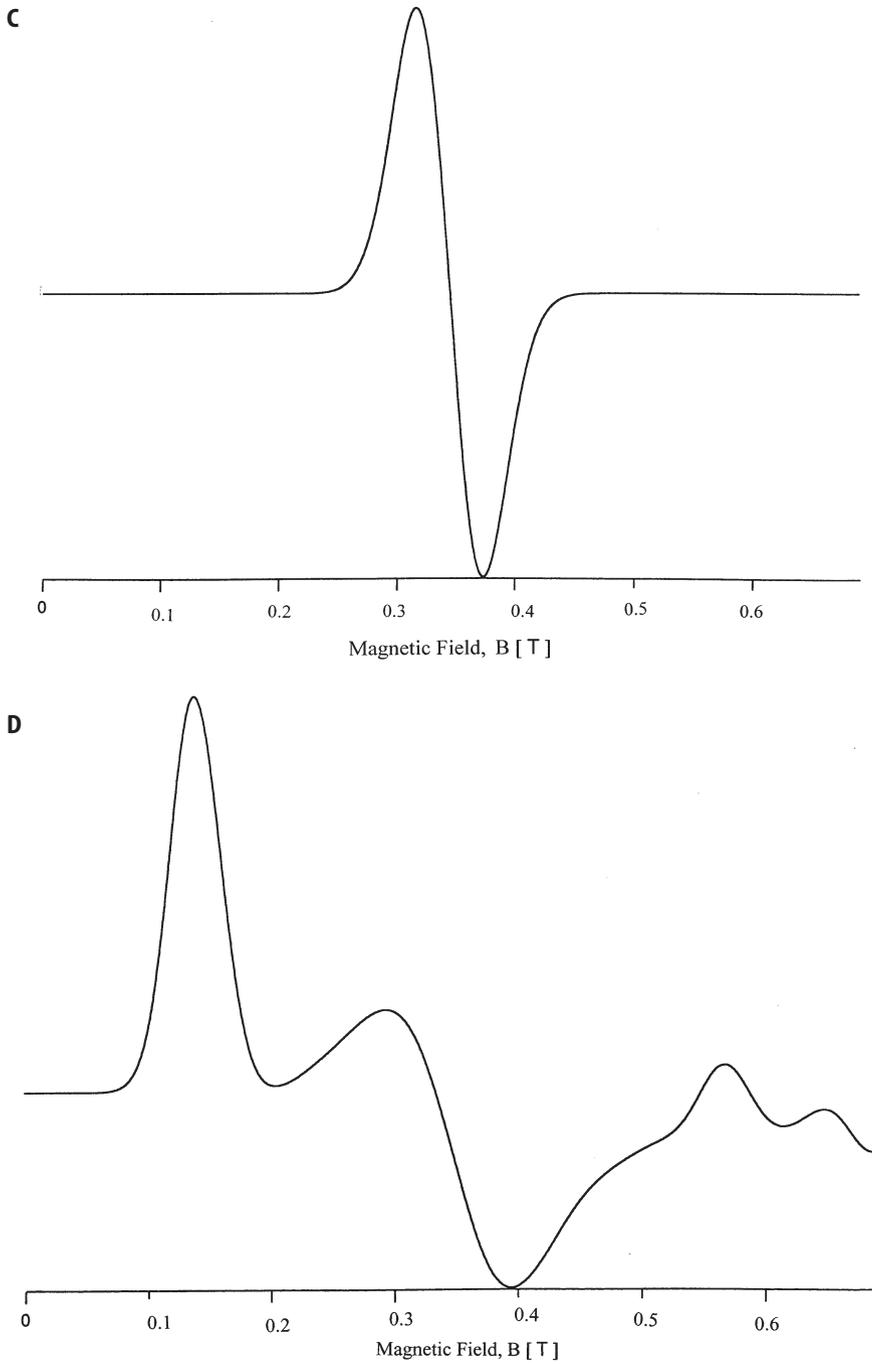**C**

Magnetic Field, B [T]

D

Magnetic Field, B [T]

Fig. 13A–D (continued). **C** theoretical spectrum with $D = E = 0$ and **D** theoretical spectrum with $D = 0.5$ cm^{-1} and $E = 0.167$ cm^{-1}

Table 4. ESR parameters of V^{4+} in vanadium containing molecular sieves

Zeolite		g-parameters	A-parameters (mT)	Reference
ZSM-5		$g_{||}$= 1.925; $g_{\perp}$=1.978	$A_{||}$=18.15; $A_{\perp}$ = 7.55	70
Silicalite		$g_{||}$= 1.932; $g_{\perp}$ =1.994	$A_{||}$=18.3; $A_{\perp}$= 6.9	70
AlPO-5	S_1	$g_{||}$= 1.939; $g_{\perp}$ = nd	$A_{||}$=18.9; $A_{\perp}$= nd	73
	resimulation of S_1	g_{xx} = 1.977; g_{yy} = 1.993; g_{zz} = 1.947	A_{xx}=7.42; A_{yy}=7.42; A_{zz} = 19.6	77
	S_2	$g_{||}$= 1.936; $g_{\perp}$=1.996	$A_{||}$=19.8; $A_{\perp}$ = 7.3	73
	resimulation of S_2	g_{xx} = 1.975; g_{yy} = 1.992; g_{zz} = 1.930	A_{xx} = 7.4; A_{yy} = 7.4; A_{zz} = 19.5	77
	L	g_{eff} = 2		77
Y		$g_{||}$= 1.941; $g_{\perp}$ = nd	$A_{||}$=20.07; $A_{\perp}$ = nd	69

3.1.4
V^{4+}

V^{4+} (d^1)-exchanged faujasite type zeolites exhibit two distinguished ESR signals and the ESR parameters are summarized in Table 4. Signal A is usually assigned to a pseudo-octahedral V^{4+}-cation located at site III in the supercage, while the second signal is attributed to square-pyramidal V^{4+} coordinated to four lattice oxygen atoms in the supercage [68, 69].

Complex overlapping ESR spectra are observed in the case of hydrothermally synthesized molecular sieves [70–77]. This is shown in Fig. 14 for as-synthesized VAPO-5 molecular sieves as a function of the V-content [77]. At low vanadium content, the spectra are characterized by two signals with hyperfine splitting due to the ^{51}V nucleus (I=$^7/_2$). These signals, denoted as S_1 and S_2, are usually considered as axially symmetric and possess slightly different g- and A-values as obtained by visual inspection of the spectra (Table 4). Furthermore, they represent only 10% of the total vanadium content [77]. At higher vanadium content, an additional broad signal (L) is formed with g_{eff} around 2.0. The L signal is due to clustered V^{4+}, while S_1 and S_2 must be due to magnetically isolated V^{4+} ions in distorted octahedral coordination. Tetrahedral coordination can be excluded because such species would have much lower A-values. There are two remarks to be made about this spectrum evaluation:

(1) No good guess of the g- and A-values is possible by eye. This is because the allowed transitions in the x, y and z directions overlap in the central region of the spectra.

(2) The relative intensities of the different allowed transitions strongly depend on the symmetry, resulting in complicated overlapping spectra.

Therefore, detailed values of g and A can only be obtained by simulation of the individual spectra S_1 and S_2, followed by an appropriate summation of the theoretical spectra. This is shown in Fig. 15, and the obtained ESR parameters are
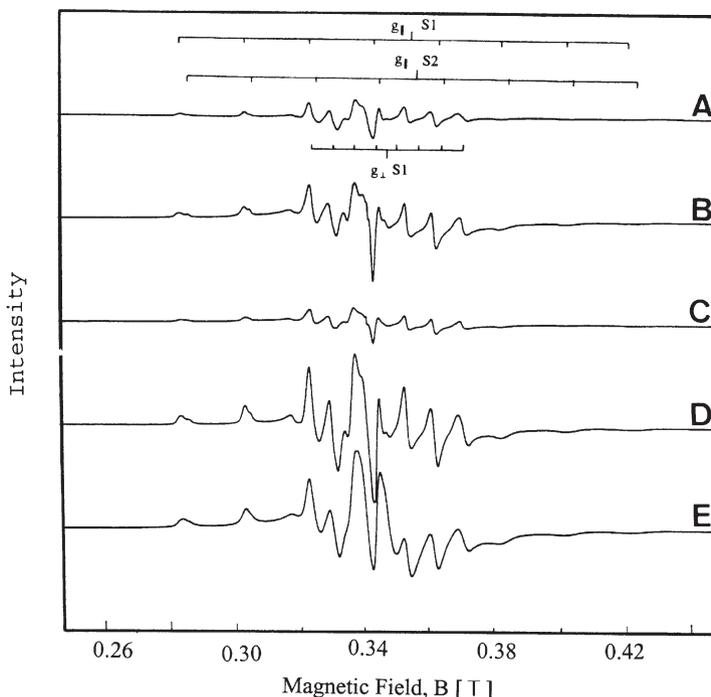
Fig. 14. ESR spectra of as-synthesised VAPO-5 molecular sieves as a function of the vanadium content (reprinted from reference [77]. Copyright 1995 Elsevier Science Publishers): gel composition $0.74R.(V_xAl_yP_1)O_4.16.7\ H_2O$ with x equal to *A* 0.01; *B* 0.02 measured at 120 K; *C* 0.02 measured at 300 K; *D* 0.04 and *E* 0.08

included in Table 4. It is clear that S_1 and S_2 are slightly rhombic and that the theoretical spectrum nicely fits the experimental one [77].

3.2
Paramagnetic Clusters and Metallic Particles

Alkali metal and Ag clusters impart not only beautiful colors to zeolites, but also give characteristic ESR signals. The latter are due to paramagnetic ionic clusters, M_n^{x+} ($n<6$) and metallic particles. This area has been pioneered by Kasai and Bishop [13]. There are several recent reviews [78, 79], which give detailed information on the preparation of these materials, the ESR signals and their interpretation. It suffices to state that the ionic clusters have been obtained in zeolites with a low Si:Al ratio and with cages: sodalite, A, X, Y, rho. Preparation methods are: (1) gamma- or X-ray irradiation [80] (2); H_2 reduction [81, 82]; (3) metal vapor adsorption [83–86]; (4) reduction with solvated electrons [87]; (5) in situ decomposition of azides [88–90]; and (6) reduction with organolithium compounds [91]. Here, attention is given to the ESR aspects of the ionic clusters and metal particles.
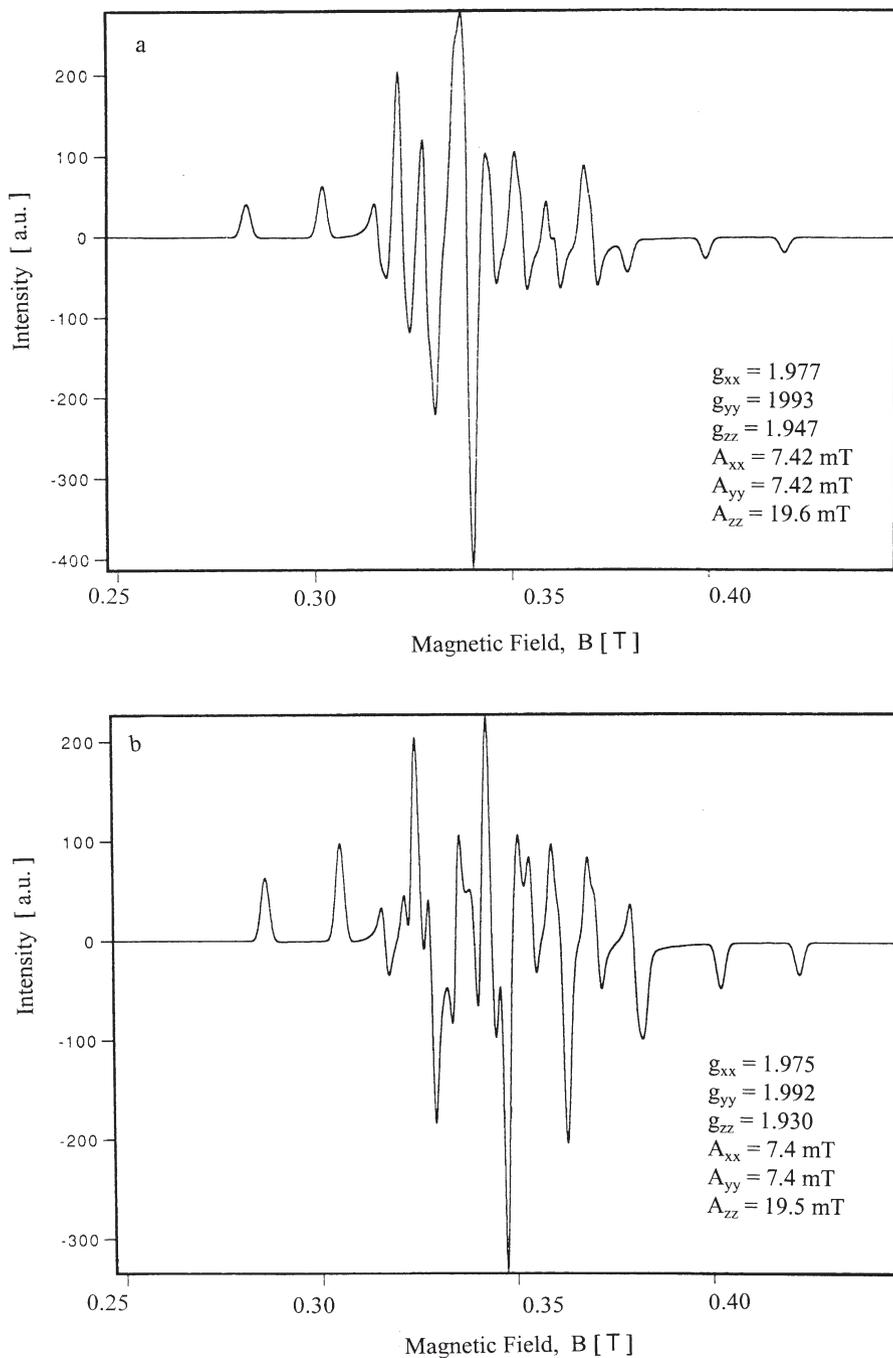
Fig. 15a–d. Simulation procedure of the ESR spectra of as-synthesised VAPO-5 molecular sieves: **a** theoretical spectrum of S_1; **b** theoretical spectrum of S_2
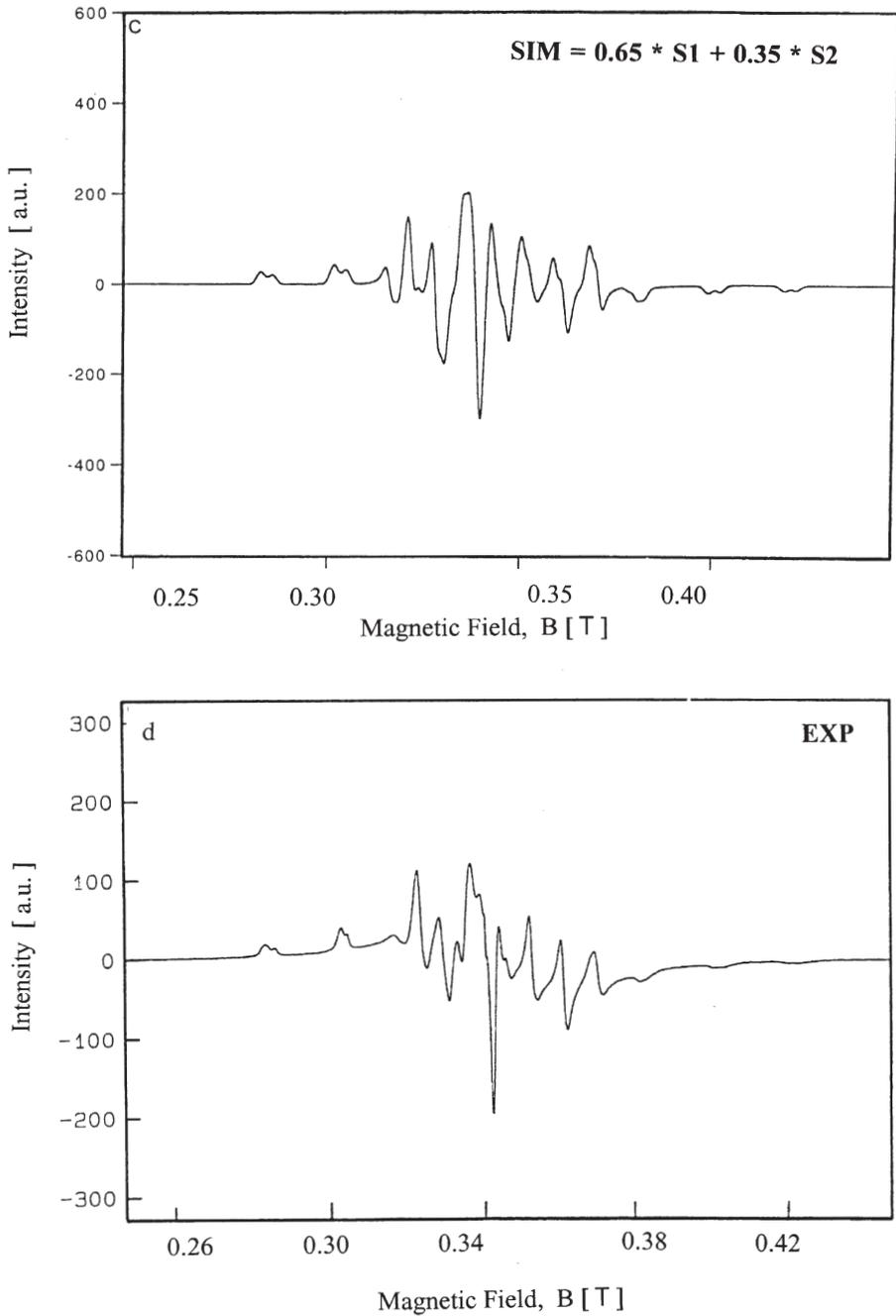
Fig. 15a–d (continued). **c** appropriate summation of the theoretical spectra of S_1 and S_2 and **d** experimental spectrum (reprinted from reference [77]. Copyright 1995 Elsevier Science Publishers)

Atoms and small nuclearity clusters, typically $n=2$ or 3, are only stable at low temperatures and are usually produced by irradiation at 77 K. The ionic clusters obtained at room temperature have higher nuclearity, $n=4–6$. While n can be directly derived from the hyperfine structure of the ESR spectra, the charge of the clusters is unknown. Most authors prefer the highest possible charge, which is 3+ for $n=4$ and 5+ for $n=6$. Such highly charged clusters are not stable in vacuum. In the zeolite, both the negative charge of the framework and confinement in the cubo-octahedra are envisaged to be responsible for the stabilization. The ESR signals have isotropic g- and A-values, suggesting that the unpaired electron is equally distributed among the n nuclei. The ratio $(nA)/A_0$ with A_0 the hyperfine splitting constant of the atom in vacuum is a measure of the distribution of the electron density over the cluster. If this number is smaller than one, it indicates the extent of delocalisation of the electron over the environment of the clusters, i.e. the zeolite matrix and surrounding cations. Values of $(nA/A_0) \times 100$ are given in Table 5. For the Na clusters the A-value depends on the type of zeolite and the type of co-exchanged cation and, when possible, ranges are indicated. The ratio $(nA/A_0) \times 100$ is larger for Ag than for Na or K, indicating that in the former case the unpaired electron is more localized than in the Na and K case. Interaction among paramagnetic ionic clusters in neighboring cages is therefore more likely for Na and K than for Ag. This can be investigated in more detail with electron spin echo modulation [92]. Thus, in the case of Na_4^{3+}, Na_6^{5+}, K_3^{2+}, K_4^{3+} and Ag_6^{5+} interaction with framework Al is evident. In addition Ag clusters of smaller nuclearity can be stabilized in the presence of solvent molecules (H_2O, CH_3OH, C_2H_5OH) even in zeolites with channel structures such as SAPO-5 and SAPO-11.

A typical Ag_6^{x+} spectrum of zeolite A is shown in Fig. 16A. Simulation with Gaussian lines gives a somewhat better fit of the experimental spectrum than simulation with a Lorentzian line shape. The g and A values are in both cases equal (Table 5). When the spectrum becomes complex, as in the case of $I > \frac{1}{2}$ nuclei, second derivative spectra are helpful in the assignment and the determination of the nuclearity (Fig. 16B).

Reduction does not stop at the ionic cluster level, but goes all the way to metallic particles. The latter is characterized by an isotropic conduction electron spin

Table 5. ESR parameters of alkali metal and silver clusters in zeolites

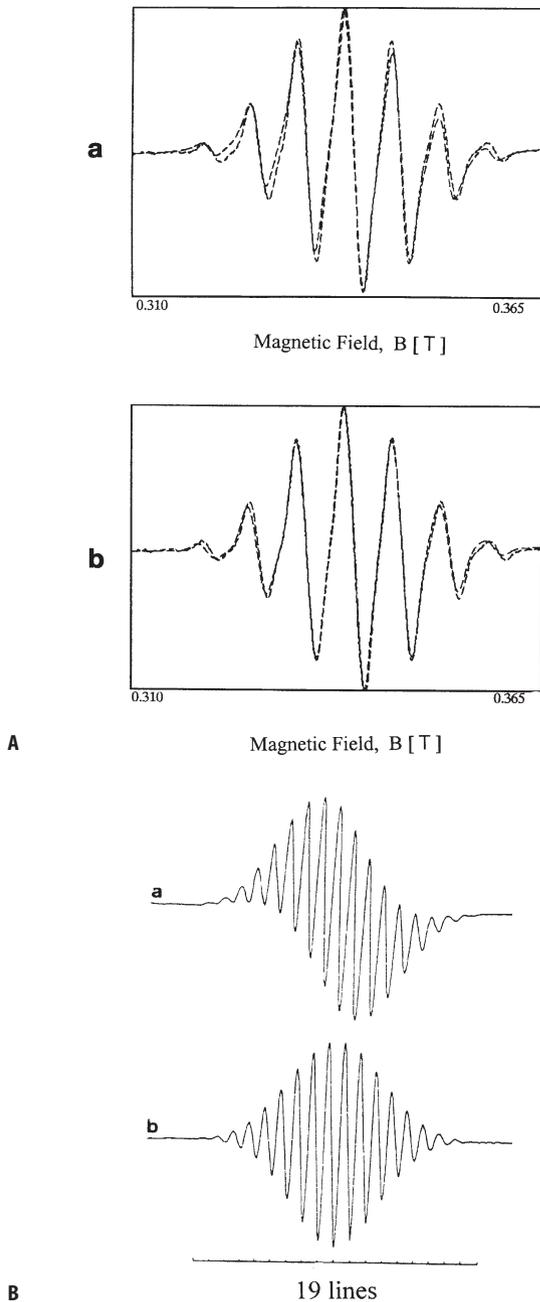| Cluster	Zeolite	g	A (mT)	$[nA/A_0] \cdot 100$ (%)	Reference
Na_4^{3+}	Y	2.0002	3.32	32–40	13, 79, 81, 83
Na_3^{2+}	X, A	2.0028	4.50	63–38	74,81
Na_5^{4+}	X	2.0022	2.50	40	80,83
Na_6^{5+}	X	2.0022	2.50	45	80,83
Ag_6^{x+}	A	1.999	6.66	56	26
Ag_4^{x+}	rho	1.973	14.0	79	76
K_3^{2+}	A	1.9992	1.28	47	78,81
Na_2^{+}	X	2.0063	8.5		74
	A	1.9983	10.0	64–46	74

Fig. 16. A Experimental and theoretical spectra of Ag_6^{x+} clusters in zeolite A: *a* Lorentzian line-shape and *b* Gaussian lineshape (reprinted from reference [36]) and **B** theoretical spectra of Na_6^{5+} clusters in zeolite X : *a* first derivative and *b* second derivative (reprinted from reference [85]. Copyright 1995 VCH Verlagsgesellschaft)

resonance (cesr) line. In many cases this line overlaps with that of the ionic clusters. A quantitative separation of both lines is only possible by simulation. This is illustrated in Fig. 17 for the sodium case. The spectra are composed of Na_4^{3+} and the cesr signal of metallic Na particles. In one case the relative contribution of the isotropic signal is 47%, in the other case 17%. The g and A values are tabulated in Table 6. It is clear that such data can only be obtained by spectral simulation, as visual inspection of the experimental spectra hardly reveals any differences.

The interpretation of the cesr signals in terms of particle size has not been attempted. All the authors notice Curie-Weiss behavior, which is indicative of quantum-sized particles [87, 89]. One is tempted to locate these particles in the supercages. The maximum diameter is then around 1.2 nm, which corresponds to 630 Li, 252 Na, 88 K, 71 Rb or 48 Cs atoms in a closed packed spherical arrangement. The line width, increasing with the size of the atom, is qualitatively explained by this decrease of the number of atoms per cluster. The g values are equal to or somewhat lower than the free electron values. The deviation is explained by spin-orbit coupling effects and thus is more pronounced for the heavier elements (Table 6).

Edwards et al. have criticized the interpretation of the $g=2$ signal in terms of quantum-sized metallic particles [78, 79, 84]. The Na signal can also be generated by exchange coupling of unpaired electrons of Na_4^{3+} clusters in neighboring cubo-octahedra. This is not unreasonable in view of the small $[nA/A_0]$ values of Table 5. The $g=2$ signal is seen at a sodium loading below occupation of all cubo-octa-hedra with Na_4^{3+}, suggesting a clustering of Na_4^{3+} instead of random distribution over available cubo-octahedra. Even Li-atoms cannot freely migrate through a six-ring into the cubo-octahedra to form the paramagnetic ionic clusters [87]. Thus, formation of an ionic cluster requires electron transfer from an atom in the supercage via the zeolitic lattice to the cations in the sodalite cage. Secondly, there must be enough cations present in the cubo-octahedra to form the cluster. If the latter is not the case, cations must migrate to the sodalite cage and this cation migration will be the rate-determining step in the ionic cluster formation. Schoonheydt and Leeman found an activation energy of 47–63 kJ $\cdot$ mol^{-1} for Ag_6^{x+} formation in zeolite A [81]. Kuranova produced the same clusters by γ-irradiation and found a complex cluster formation mechanism with activation energies in the range 19–30 kJ $\cdot$ mol^{-1} and rate constants of 58–5300$\times 10^{-6}$ s^{-1} at 293 K [91]. Because of the two different cluster production techniques the activation energies might not be comparable, but both point to cationic migration [93]. Clearly, research into the mechanism and kinetics of cluster formation is valuable and promising.

3.3
Paramagnetic Molecules

Molecular sieves can be used to isolate and to store stable paramagnetic molecules. These stable radicals can then be used to study Lewis acidity and exchangeable cations. We will limit our discussion to ESR studies of NO as a probe molecule. Details about the ESR results of other paramagnetic molecules, like NO_2, NF_2 and ClO_2 can be found in a review of Kasai and Bishop [13].
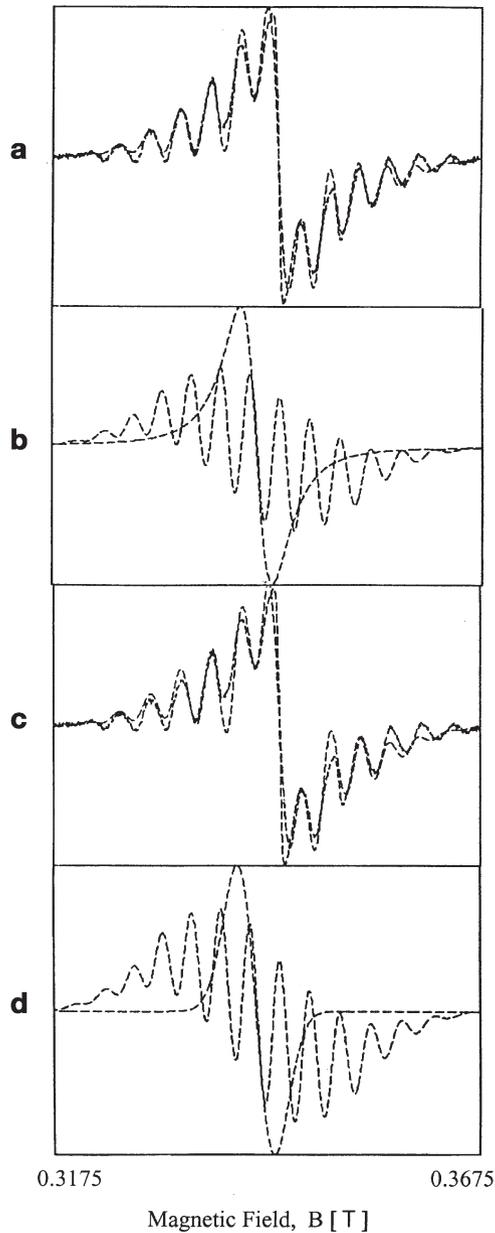
Fig. 17a–d. ESR spectra of zeolitic sodium clusters in zeolite Y: **a** experimental and theoretical spectrum obtained by a summation of the two signals of (**b**); **b** the ionic cluster, characterized by a 13-line spectrum, is simulated using a Gaussian lineshape, whereas the metallic cluster with an isotropic signal has a Lorentzian lineshape; **c** experimental and theoretical spectrum obtained by a summation of the two signals of (**d**); **d** the ionic cluster is simulated using a Gaussian lineshape, whereas the metallic cluster is now also simulated with a Gaussian line-shape (reprinted from reference [36])

Table 6. Conduction electron spin resonance signals in zeolite X and Y

Metal	Zeolite	g	Linewidth (mT)	Remark	Reference
Na	X	2.0016	0.43	NaN_3	82
		2.0011		Na vapour	79
Na	Y	2.0002	0.82	NaN_3	83
		2.0014		Na vapour	79
Na	A	2.0014		Na vapour	79
Na	A	2.0005		Na vapour	79
K	X	1.9997	0.58	KN_3	82
Rb	X	1.9929	0.76	RbN_3	82
Cs	X	1.9686	2.13	CsN_3	82

NO is a stable paramagnetic molecule, which exhibits, in spite of its unpaired electron in the free molecule, no paramagnetism in its $^2p_{1/2}$ ground state. This is due to the degeneracy of the orbitals which leads to cancellation of the spin magnetic moment of the electron by its orbital magnetic moment. The ESR spectrum of this system should become observable if the orbital moment of the electron is quenched. Thus, the degeneracy among the p orbitals should be removed by its environment. This can be induced by the electric field associated with zeolitic cations. This is illustrated in Fig. 18. The z axis is identified with the N-O internuclear direction, and the zeolitic cation is placed in the y-x plane. The unpaired electron resides in the antibonding π_y^* orbital. One has to cool the zeolite sample down to low temperature to obtain the corresponding ESR spectrum. The spectrum originates from interaction of the unpaired electron of the NO molecule with the cation, while the observed hyperfine structure indicates the interaction of the unpaired electron with the ^{14}N atom with $I=1$. An example of such a spectrum is given in Fig. 19 for NO-treated Na-Y. The corresponding g tensors,
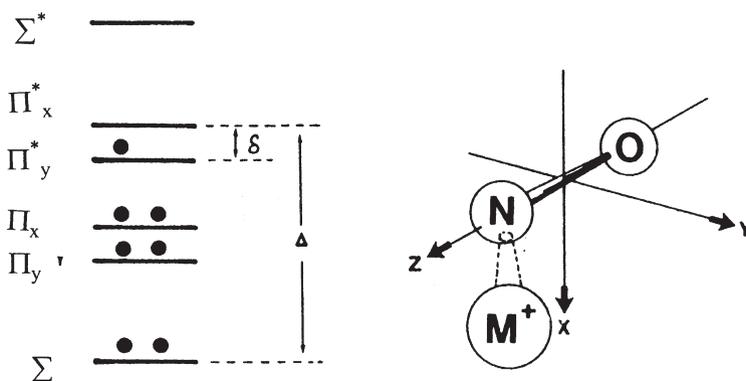

Fig. 18. Valence orbitals of NO adsorbed on a cation with a bent structure (reprinted from reference [13]. Copyright 1976 American Chemical Society)
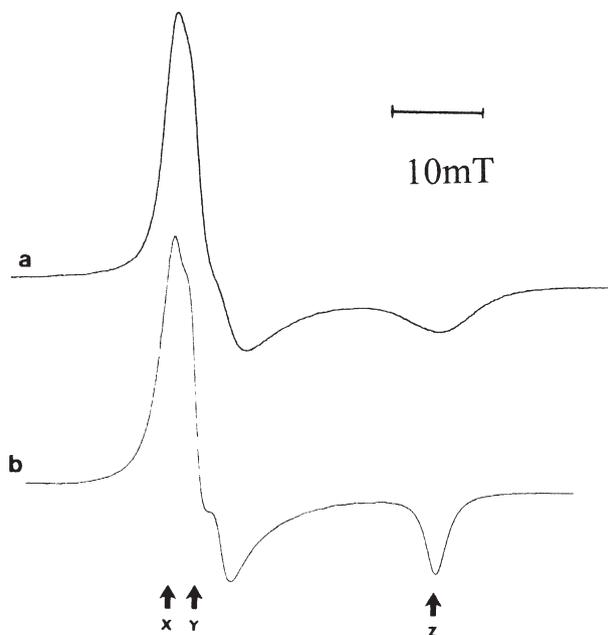
Fig. 19a, b. ESR spectrum of NO adsorbed on NO-treated NaY (reprinted from reference [13]. Copyright 1976 American Chemical Society): **a** experimental and **b** theoretical spectrum

the hyperfine coupling tensors A_N, and the π orbital separations (δ in Fig. 18) for a series of NO-treated Na-X, Na-Y and Ba-Y are given in Table 7.

An additional interaction is observed if aluminum containing extra-framework cations or Lewis acid sites are present. Due to the nuclear spin of Al ($I = {}^5/_2$), each nitrogen hyperfine line is split into six lines, some of which may overlap. An example of such interaction is shown in Fig. 20 for NO-treated H-ZSM-5. Witzel et al. have used this property to determine the density and acidity of Lewis sites in H-ZSM-5, H-Mordenite and H-Y zeolites [94–95]. The results obtained are in good agreement with those of more conventional methods and, consequently, ESR spectroscopy with NO as probe is a valuable tool for studying Lewis acidity in zeolites. It is important to stress that ESR spectroscopy of adsorbed NO is only

Table 7. The g tensors, the hyperfine coupling tensors A (mT) and the π orbital separations S (eV) in NO-treated X and Y zeolites (the z axis is parallel to the N-O bond, as shown in Fig. 18) [13]

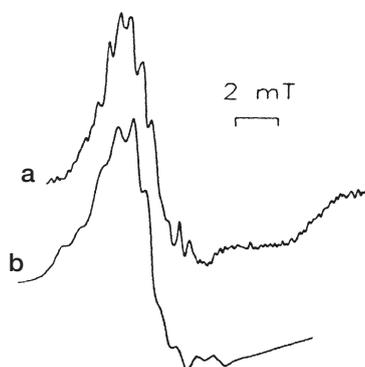| Zeolite	g_{xx}	g_{yy}	g_{zz}	A_{xx}	A_{yy}/mT	A_{zz}	δ
NaX	1.970	1.970	1.790	0	2.9	0	0.09
NaY	1.999	1.995	1.830	0	3.4	0	0.12
BaY	2.000	1.998	1.890	0	3.0	0	0.18

Fig. 20a, b. ESR spectrum of NO adsorbed on NO-treated H-ZSM-5 (reprinted from reference [94]. Copyright 1992 VDI Verlag): **a** experimental and **b** theoretical spectrum

probing the sites strong enough to quench the orbital magnetic moment of the NO molecule and other methods should be called in to give a more global picture of the Lewis acidity of a particular zeolite sample [96]. The ESR method, however, can provide an estimation of the strength of the detected Lewis acid sites, via the g_{zz} parameter. The stronger the electric field of the Lewis acid site, the smaller the difference $\Delta g_{zz} = g_e - g_{zz}$, where g_e is the free electron value (2.0023).

Paramagnetic molecules can also be generated inside the zeolite cavities by using ionizing γ- and X-ray radiation. The most studied molecules are O_2^- and Cl_2^-, but other anion radicals such as SO_2^- and CO_2^- can also be generated inside zeolites. The super-oxide ion O_2^- is obtained by interaction of O_2 with transition metal ions and their complexes in zeolites. While NO is a one electron system, O_2^- is a one hole system. Thus both molecules have similar ESR spectra with $g < 2.0023$ for NO and $g > 2.0023$ for O_2^- (see Tables 7 and 8). If the O_2^- is coordinated to transition metal ions such as Co^{2+}, typical hyperfine patterns are seen if the transition metal ion has a nuclear spin $I \neq 0$ [97].

4
General Conclusions and Outlook

Electron spin resonance is a very sensitive and powerful technique to probe the electronic structures of paramagnetic entities in molecular sieves. There is a vari-

Table 8. The g tensors and π orbital separations of δ (eV) O_2^- generated in zeolites by ionizing radiations (the z axis is parallel to the O-O bond) [13]

Zeolite	g_{xx}	g_{yy}	g_{zz}	δ (eV)
NaX	2.0000	2.0048	2.162	0.18
NaY	2.0016	2.0066	2.080	0.36
BaY	2.0046	2.0090	2.057	0.51

ety of ESR techniques available, each with their particular advantages and limitations. CW X-band ESR spectroscopy is the most popular technique because of its availability, although there is now an increasing use of more advanced techniques such as ENDOR and ESEEM. In addition, multi-frequency and high frequency ESR, such as CW W-band ESR, will be very useful in detailed analysis of coordination environments of transition metal ions.

The various ESR techniques can be applied at different levels of sophistication: from merely detecting the presence of paramagnetic species over the determination of the first coordination sphere around the paramagnetic center up to a detailed description of the electronic structure. Whatever level is being considered, it is important that the user realizes both the potential and the limitations of the particular technique. Over-interpretation should certainly be avoided. This holds equally so for under-interpretation, if with some extra effort (e.g. spectrum simulations), more physically meaningful information can be extracted from the experimental spectra. The systematic and intelligent application of ESR and its related techniques will therefore lead in the future to a better understanding of paramagnetic entities in molecular sieves.

5
References

1. Abragam A, Bleaney B (1970) Electron paramagnetic resonance of transition metal ions. Clarendon Press, Oxford
2. Pilbrow JR (1990) Transition Ion Electron Paramagnetic Resonance. Clarendon Press, Oxford
3. Atherton NM (1973) Electron spin resonance, theory and applications. Ellis Horwood, Chichester
4. Wertz JE, Bolton JR (1986) Electron spin resonance, elementary theory and practical applications. Chapman and Hall, New York
5. Mabbs FE, Collison D (1992) Electron Paramagnetic Resonance of Transition Metal Compounds. Elsevier, Amsterdam
6. Poole CP (1967) Electron spin resonance: a comprehensive treatise on experimental techniques. Interscience Publishers, a division of John Wiley, New York
7. Wilmshurst TH (1967) Electron spin resonance spectrometers. Hilger, London
8. Weckhuysen BM, Van Der Voort P, Catana G (eds) (2000) Spectroscopy of transition metal ions on surfaces. Leuven University Press, Leuven
9. Hyde JS, Froncisz W (1981) Specialist Periodical Reports: Electron Spin Resonance. Royal Society of Chemistry, Vol 10
10. Vedrine JC (1984) In: Delannay F (ed) Characterization of Heterogeneous Catalysts. Marcel Dekker, New York, p 161
11. Mabbs FE (1993) Chem Soc Rev: 314
12. Lunsford JH (1972) Adv Catal 22:265
13. Kasai PH., Bishop RJ (1976) In: Rabo JA (ed) Zeolite Chemistry and Catalysis. ACS Monograph 171, American Chemical Society, Washington, DC, p 350
14. McGarvey BR (1966) Transit Metal Chem 3:89
15. Weber RT (1992) ESP 300 E EPR Spectrometer User's Manual, Bruker Instruments, Inc, Billerica, Massachusetts, USA

16. Weckhuysen BM, Schoonheydt RA (1994) Stud Surf Sci Catal 84:965
17. Schweiger A (1991) Angew Chem 103:223
18. Mims WB (1972) In: Geschwind S (ed) Electron Paramagnetic Resonance. Plenum Press, New York 4:263
19. Heming M (1987) Z Phys Chem Neue Folge 151:35
20. Mehring M (1987) Z Phys Chem Neue Folge 151:1
21. Martini G (1990) Colloids and Surfaces 45:83
22. Kevan L, Bowman MK (1990) Modern Pulsed and Continuous Wave Electron Spin Resonance. Wiley, New York
23. Drago RA (1997) Physical Methods in Chemistry. E.B. Saunders Comp., Philadelphia, p 319
24. Ingram DJE (1956) Free Radicals Studied by Electron Spin Resonance. Butterworths, London, p 95
25. Dedecek J, Sobalik Z, Tvaruzkova Z, Kaucky D, Wichterlova B (1995) J Phys Chem 99: 16327
26. Schoonheydt RA (1993) Catal Rev-Sci Eng 35:129
27. Packet D (1987) PhD Thesis, Faculty of Applied Biological Sciences Nr 151, KULeuven
28. De Tavernier S (1989) PhD Thesis, Faculty of Applied Biological Sciences Nr 182, KULeuven
29. Schoonheydt RA (1989) J Phys Chem Solids 50:523
30. Chen X, Kevan L (1991) J. Am. Chem. Soc. 113:2861
31. Lee CW, Chen X, Kevan L (1992) Catal Lett 15:75
32. Lee CW, Chen X, Kevan L (1991) J Phys Chem 95:8626
33. Lee CW, Chen X, Kevan L (1992) J Phys Chem 96:358
34. Lee CW, Brouet G, Chen X, Kevan L (1993) Zeolites 13:565
35. Lee CW, Kevan L (1994) Zeolites 14:267
36. Uyttterhoeven M (1989) Optimalisatie van ESR poederspektra, Master of Engineering thesis, KULeuven;
37. Uytterhoeven MG, Schoonheydt RA (1991) In: Jacobs PA, Jaeger NI, Kubelkov, L, Wichterlov B (eds) Zeolite Chemistry and Catalysis, Proc. Int. Symp., Prague, Szecho-Slovakia, Sept. 8–13, 1991 Elsevier, Amsterdam, 1991; Stud Surf Sci Catal 69:443
38. Heidler R, Janssens GOA, Mortier WJ, Schoonheydt RA (1996) J Phys Chem 100:19728
39. Pierloot K, Delabie A, Ribbing C, Verberckmoes AA, Schoonheydt RA (1998) J Phys Chem 102:10789
40. Delabie A, Pierloot K, Groothaert MH, Weckhuysen BM, Schoonheydt RA (2000) Micropor Mesopor Mater 37:209
41. Pierloot K, Delabie A, Groothaert MH, Schoonheydt RA (2001) Phys Chem Chem Phys 3:2174
42. Sass CE, Kevan L (1988) J Phys Chem 32:5192
43. Anderson MW, Kevan L (1987) J Phys Chem 91:2926
44. Brown DR, Kevan L (1988) J Phys Chem 92:1971
45. Poppl A, Baglioni P, Kevan L (1995) J Phys Chem 99:14156
46. Poppl A, Hartmann M, Kevan L (1995) J Phys Chem 99:17251
47. Weckhuysen BM, Verberckmoes AA, Vannijvel IP, Pelgrims JA, Buskens PL, Jacobs PA, Schoonheydt RA (1995) Angew Chem Int Ed Engl 34:2652; Weckhuysen BM, Verberckmoes AA, Fu L, Schoonheydt RA (1996) J Phys Chem 100:9456
48. Grommen R, Manikandan P, Gao Y, Shane T, Shane JJ, Schoonheydt RA, Weckhuysen BM, Goldfarb D (2000) J Am Chem Soc 122:11488
49. McNicol BD, Pott GT (1972) J Catal 25:223
50. Derouane EG, Mestdagh M, Vielvoye I (1974) J Catal 33:169
51. Ratnasami P, Kumar R (1991) Catal Today 9, 328
52. Lin DH, Coudurier G, Vedrine J (1989) In: Jacobs PA, van Santen, R (eds) Zeolites: Facts, Figures and Future, Proc 8th Int Zeolite Conf, Amsterdam, The Netherlands, July 10–14 1989 Elsevier, Amsterdam; Stud Surf Sci Catal 49:1431
53. Goldfarb D, Bernardo M, Strohmaier KG, Vaughan DEW, Thomann H (1994) J Am Chem Soc 116:6344

54. Goldfarb D, Bernardo M, Strohmaier KG, Vaughan DEW, Thomann H (1994) Stud Surf Sci Catal 84:403
55. Kucherov AV, Slinkin AA (1988) Zeolites 8:110
56. Catana G, Pelgrims J, Schoonheydt RA (1995) Zeolites 15:475
57. Uytterhoeven M (1995) PhD Thesis, Faculty of Applied Biological Sciences Nr 293, KU Leuven
58. Hemidy JF, Delavennat F, Cornet D (1973) J Chim Phys 11–12:1716
59. Hemidy JF, Goupil JM, Cornet D (1977) J Chim Phys 7:71
60. Hemidy JF, Cornet D (1974) J Chim Phys 5:739
61. Pearce JR, Sherwood DE, Hall MB, Lunsford JH (1980) J Phys Chem 84:3215
62. Kucherov AV, Slinkin AA (1994) J Mol Catal 90:323
63. Weckhuysen BM, Schoonheydt RA, Mabbs FE, Collison D (1996) J Chem Soc Faraday Trans 92:2431
64. Huang M, Deng Z, Wang Q (1990) Zeolites 10:272
65. Weckhuysen BM, Schoonheydt RA (1994) Zeolites 14:360
66. Nakumura O, Mambrim JS, Pastore HO, Vichi EJS, Gandra FG, Silva EC, Vargas H, Pelzi J (1992) J Chem Soc Faraday Trans 88:2071
67. Weckhuysen BM, Wachs IE, Schoonheydt RA (1996) Chem Rev 96:3327
68. Martini G, Ottaviani MF, Servavalli GL (1975) J Phys Chem 79:1716
69. Fricke R, Selenina M, Schnabel KH (1976) Z Phys Chemie, Leipzig Z57:968
70. Whittington BI, Anderson JR (1993) J Phys Chem 97:1032
71. Centi G, Perathorer S, Trifiro F, Aboukais A, Aissi CF, Guelton M (1992) J Phys Chem 96:2617
72. Petras M, Wichterlova B (1992) J Phys Chem 96:1805
73. Rigutto MS, van Bekkum H (1993) J Mol Catal 81:77
74. Montes C, Davis ME, Murray B, Naryana M (1990) J Phys Chem 94:6425
75. Jhung SH, Uh YS, Chon H (1990) Appl Catal 62:61
76. Rao PRHP, Ramaswamy AV, Ratnasamy P (1992) J Catal 137:225
77. Weckhuysen BM, Vannijvel IP, Schoonheydt RA (1995) Zeolites 15:482
78. Edwards PP, Woodall LJ, Anderson PA, Armstrong AR, Slaski M (1993) Chem Soc Rev:305
79. Edward PP, Anderson PA, Thomas JM (1996) Acc Chem Res 29:23
80. Liu X, Thomas JK (1992) Chem Phys Lett 192:555
81. Schoonheydt RA, Leeman H (1989) J Phys Chem 93:2048
82. Xu B, Kevan L (1991) J Phys Chem 95:1147
83. Anderson PA, Singer RJ, Edwards PP (1991) J Chem Soc Chem Commun: 914
84. Anderson PA, Edwards PP (1992) J Am Chem Soc 114:10608
85. Anderson PA, Edwards PP (1991) J Chem Soc Chem Comm:915
86. Anderson PA, Barr D, Edwards PP (1991) Angew Chem 103:1511
87. Xu B, Kevan L (1992) J Phys Chem 96:2642
88. Grobet PJ, Martens LRM, Vermeiren WJH, Huybrechts, DRC, Jacobs PA (1989) Z Phys D – Atoms, Molecules, Clusters 12:37
89. Blazey KW, Muller KA, Blatter F, Schumacher E (1987) Europhysics Letters 4:857
90. Yoon KB, Kochi JK (1988) J Chem Soc Chem Comm: 510
91. Kuranova GA (1990) Russian J Phys Chem 64:833
92. Michalik J, Wasowicz T, Sadlo J, Reijerse EJ, Kevan L (1995) Radiat Phys Chem 47:75
93. Mortier WJ, Schoonheydt RA (1985) Progress Solid State Chem 16:1
94. Witzel F, Karge HG, Gutsze A (1993) Proc 9th Int Zeolite Conf, Montreal, Canada, July 5–10, 1992 (von Ballmoos R, Higgins JB, Treacy MMJ, eds) Butterworth-Heinemann, London, 283
95. Gutsze A, Plato M, Karge HG, Witzel F (1996) J Chem Soc Faraday Trans 92:2495
96. Catana G, Baetens D, Mommaerts T, Schoonheydt RA, Weckhuysen BM (2001) J Phys Chem B 105:4904
97. De Vos DE, Thibault-Starzyk F, Jacobs PA (1994) Angew Chem 106:447